

# AGN activity and nuclear starbursts: Sgr A\* activity shapes the Central Molecular Zone

Kastytis Zubovas

*Center for Physical Sciences and Technology, Savanorių 231, Vilnius LT-02300, Lithuania*

*E-mail:* kastytis.zubovas@ftmc.lt

11 June 2021

## ABSTRACT

The Central Molecular Zone (CMZ) of the Milky Way shows several peculiar properties: a large star formation rate, some of the most massive young star clusters and molecular clouds in the Galaxy, and a twisted ring morphology in molecular gas. In this paper, I use SPH simulations to show that most of these properties can be explained as due to a recent outburst of AGN activity in Sgr A\*, the central supermassive black hole of the Milky Way. In particular, the narrow ring of dense gas, massive gas clouds, young star clusters and an elevated SFR can all be caused by the passage of an AGN outflow through the system, which compresses the gas and triggers fragmentation. Furthermore, I show that the asymmetric distribution of gas, as observed in the CMZ, can be produced by outflow-induced instabilities from an initially axisymmetric gas disc. Angular momentum mixing in the disc produces some low angular momentum material, which can subsequently feed Sgr A\*. These processes can occur in any galaxy that experiences an AGN episode, leading to bursts of nuclear star formation much stronger than pure bar-driven mass inflows would predict.

**Key words:** quasars: general — accretion, accretion discs — ISM: evolution — Galaxy: centre — stars: formation — open clusters and associations: general

## 1 INTRODUCTION

Over the past two decades, various observations revealed that most galaxies harbour supermassive black holes (SMBHs) at their centres (Kormendy & Richstone 1995; Magorrian et al. 1998). It is expected that these SMBHs and their immediate surroundings spend a few percent of their lifetimes as active galactic nuclei (AGNs), accreting gas at rates exceeding a few percent of their Eddington limit  $\dot{M}_{\text{Edd}} = 2.2 \times 10^{-8} (M_{\text{BH}}/M_{\odot}) M_{\odot} \text{ yr}^{-1}$ . During this time, the AGN luminosity can exceed that of the whole host galaxy. The AGN radiation can heat the surrounding gas by photoionization and Compton heating. More importantly, quasi-relativistic winds (Tombesi et al. 2010b, 2014) and massive molecular outflows (Sturm et al. 2011; Cicone et al. 2014, 2015) have been detected in AGN, the latter most likely driven by the former (Tombesi et al. 2015). The observed outflow energy rate is  $\sim 5\%$  of the AGN luminosity, as predicted by analytical (Zubovas & King 2012) and numerical (Costa et al. 2014, 2015) models. Such outflows affect the AGN host galaxy on scales ranging from the immediate AGN environment to the circumgalactic medium. Importantly, footprints of these effects can remain visible for a much longer time than the duration of the AGN phase

itself, allowing us to probe the past activity of presently quiescent galactic nuclei.

A prototypical and well-studied quiescent galactic nucleus is our own Galactic Centre (GC), which contains a radio source Sgr A\*, identified as an  $M_{\text{BH}} = 4.3 \times 10^6 M_{\odot}$  SMBH (Ghez et al. 2008; Gillessen et al. 2009). The current bolometric luminosity of Sgr A\* is very low,  $L_{\text{bol}} \sim 300 L_{\odot} \sim 10^{-9} L_{\text{Edd}}$  (e.g., Melia & Falcke 2001). There is evidence that this low luminosity is caused by two effects: there is little gas supplied into the several-pc wide sphere of influence around Sgr A\* (Bower et al. 2003; Marrone et al. 2006), and the gas that is supplied is accreted with very low efficiency (Wang et al. 2013).

However, there is growing evidence that Sgr A\* used to be much brighter in the past. Light echoes from molecular clouds in the Galactic centre reveal that Sgr A\* X-ray luminosity was  $L_{\text{X}} \sim 10^{39} \text{ erg s}^{-1}$  about 100 years ago (Revnivtsev et al. 2004; Terrier et al. 2010) and perhaps on several other occasions in the past  $\sim 10^3$  years (Gando Ryu et al. 2012). On longer timescales, there is evidence of significant activity some time during the past 10 Myr. This evidence comes from the presence of young stars in the central parsec (Paumard et al. 2006; Hobbs & Nayakshin 2009) and the two large gamma-ray

emitting bubbles (the *Fermi* bubbles; Su et al. 2010), which have properties consistent with being inflated several Myr ago by either an AGN jet (Guo & Mathews 2012) or wind-driven outflow (Zubovas et al. 2011; Zubovas & Nayakshin 2012, also see Section 2 below). In particular, in these two papers my colleagues and I showed that an Eddington-limited AGN outburst that started 6 Myr ago and lasted for 1 Myr would have produced two bubbles with sizes, shapes and energy content consistent with observations.

Given this evidence of increased past activity, it is interesting to check whether footprints of that activity might be present closer to the GC, such as in the Central Molecular Zone (CMZ) of the Galaxy. The CMZ is a ring-like structure of predominantly molecular gas (Morris & Serabyn 1996; Jones et al. 2011; Molinari et al. 2011). It is oriented parallel to the plane of the Galaxy, with a radius  $R_{\text{CMZ}} \sim 200$  pc and thickness  $h_{\text{CMZ}} \sim 100$  pc (Morris & Serabyn 1996), giving an approximate aspect ratio  $H/R \simeq 0.25$ . The total gas mass contained in this region is  $M_{\text{CMZ}} \sim 10^8 M_{\odot}$  (Morris & Serabyn 1996; Pierce-Price et al. 2000; Molinari et al. 2011).

The CMZ contains several star formation regions, such as the molecular cloud Sgr B2 (the most massive GMC in the Galaxy;  $M_{\text{SgrB2}} \simeq 2 \times 10^6 M_{\odot}$ ; Reznivtsev et al. 2004), Sgr C and Sgr D (Pierce-Price et al. 2000). Two young massive star clusters, Arches ( $t_{\text{age}} \simeq 3 \pm 1$  Myr,  $M \simeq 4 - 7 \times 10^4 M_{\odot}$ , Martins et al. 2008; Portegies Zwart et al. 2002; Figer et al. 2002) and Quintuplet ( $t_{\text{age}} \simeq 4 \pm 1$  Myr,  $M \simeq 10^4 M_{\odot}$ , Figer et al. 1999) are also associated with the region. The mean star formation rate in the region,  $\dot{M}_{\star} \sim 0.06 - 0.08 M_{\odot} \text{ yr}^{-1}$  (Yusef-Zadeh et al. 2009; Immer et al. 2012; Longmore et al. 2013), would deplete the molecular gas reservoir in  $t_{\text{dep}} \sim 10^9 \text{ yr} \ll t_{\text{Galaxy}} \sim 10^{10} \text{ yr}$ , therefore it seems likely that the present star formation rate is elevated by some recent process, i.e. one that occurred at most a few dynamical times ago (see, however, Rodriguez-Fernandez & Combes 2008, who show that the elevated star formation rate can be maintained by material transport via bars from further out in the MW).

Recent *Herschel* observations reveal a complex structure of numerous clouds and filaments comprising the CMZ (Molinari et al. 2011). They are mostly positioned on a narrow elliptical ring, which is twisted and offset from the dynamical centre of the Galaxy. The line-of-sight velocities of the clouds are larger than would be expected if the gas was moving along the ring. In particular, the “20 km/s” and “50 km/s” clouds certainly do not follow the ring. Therefore the ring is most likely just a transient structure, created by an accidental accumulation of gas.

In this paper, I present numerical simulations designed to show what effect a recent burst of AGN activity in Sgr A\* might have had upon the CMZ properties. Starting from idealised initial conditions, the AGN wind shapes the CMZ into its present-day elliptical configuration and triggers gravitational instabilities which lead to formation of massive young star clusters. The overall conclusion is that AGN activity might be as important a factor in CMZ evolution as the perturbation due to the bar potential of the Galaxy.

The paper is structured as follows. I briefly review the AGN wind-driven outflow model and derive the important quantities regarding its effect upon the cold CMZ gas in section 2. Then, I describe the numerical simulation setup

(section 3) and present their results (section 4), paying particular attention to the morphology of the gas and orbits of star clusters, the star formation rate and the global properties of the star cluster population. I discuss the main implications of these results in section 5 and summarize them in section 6.

## 2 AGN WINDS AND THEIR EFFECT ON DENSE GAS

### 2.1 Wind feedback model

Observations show that a large fraction of AGN have fast ( $v_w \sim 0.1c$ ) winds with kinetic power  $L_{\text{kin}} \sim 0.05 L_{\text{AGN}}$  (Tombesi et al. 010a,b). The ubiquity of observed winds suggests that they are emitted with a wide opening angle, perhaps quasi-spherically (Nardini et al. 2015). These winds shock against the galactic ISM and drive large-scale outflows (King 2010). In principle, if the shock occurs very close to the SMBH, the inverse-Compton cooling allows the wind to rapidly lose most of its energy and the resultant flow is momentum-driven (King 2003). However, in practice, the electron-ion thermalisation timescale in the two-temperature plasma of the shocked wind is long enough so that cooling is efficient only at distances  $< 1$  pc from the AGN (Faucher-Giguère & Quataert 2012) and the outflows are essentially always energy-driven. Nevertheless, in a non-uniform ISM, most of the outflow energy leaks out through low-density channels, effectively recovering the momentum-driven solution for the dense gas (Nayakshin 2014; Zubovas & Nayakshin 2014; Gabor & Bournaud 2014). Such outflows are then good candidates for communicating the AGN luminosity to the host galaxy and establishing the  $M - \sigma$  relation (King 2003, 2010). The ram pressure of the wind can only push away dense gas if the AGN luminosity is higher than the critical value  $L_{\sigma} \sim 3 \times 10^{45} \sigma_{100}^4 \text{ erg s}^{-1}$ , where  $\sigma \equiv 100 \sigma_{100} \text{ km/s}$  is the velocity dispersion in the host galaxy. Assuming the AGN to be Eddington-limited, this translates into a minimum mass  $M_{\sigma} \sim 2.3 \times 10^7 \sigma_{100}^4 M_{\odot}$ .

In our Galactic centre, one then expects that any outflow would affect the CMZ predominantly via the ram pressure of the wind. This pressure exerts a force

$$\dot{p} = \frac{L}{c} \lesssim \frac{4\pi G M_{\text{SMBH}}}{\kappa_e} \simeq 1.8 \times 10^{34} \text{ dyn}, \quad (1)$$

where I used the value of Sgr A\* mass  $M = 4.3 \times 10^6 M_{\odot}$  (Ghez et al. 2008; Gillessen et al. 2009). In comparison, the weight of the CMZ is

$$W_{\text{CMZ}} \simeq \frac{G M_{\text{CMZ}} M (< R_{\text{CMZ}})}{R_{\text{CMZ}}^2} \simeq \frac{M_{\text{CMZ}} \sigma^2}{R_{\text{CMZ}}} \simeq 3 \times 10^{34} M_8 \sigma_{100}^2 R_{200}^{-1} \text{ dyn}, \quad (2)$$

We see that even an Eddington-limited outburst from Sgr A\* is unable to lift the CMZ and remove it from the Galaxy. Note, however, that the difference between the two quantities is only a factor  $\sim 2$ , so even a modest retention of the outflow energy (rather than just its momentum) can disperse the CMZ. This may lead to the CMZ being eroded over a longer timescale, as its surface material absorbs some of the outflow energy, heats up and evaporates.

## 2.2 Mixing of CMZ material

Even though the CMZ is not dispersed, the AGN wind can significantly perturb it. The ram pressure is not negligible compared to the weight of the whole CMZ, so a significant fraction of the CMZ material is pushed outwards and can mix with the rest.

The CMZ is located outside the sphere of influence of the SMBH, so the circular velocity of its components is approximately independent of radius. Hence the specific angular momentum of CMZ gas increases linearly with radius and spans more than an order of magnitude. When gas with different angular momentum is mixed together, the result is an averaging of this quantity (Hobbs et al. 2011). Gas injected from the centre gains angular momentum, while gas from outside loses it, in a process similar to a time-inverted viscous ring evolution (except that the process responsible for the mixing of angular momentum is dynamical perturbations rather than viscosity). We can make a rough estimate of the radius at which the CMZ gas would collect after this perturbation. If we assume the CMZ follows an  $R^{-2}$  radial density profile with constant  $H/R$ , the mass at each radius is just  $M(R \rightarrow R + \Delta R) = M_{\text{CMZ}} \Delta R / R_{\text{CMZ}}$ . If the CMZ is affected out to radius  $R_{\text{out}} < R_{\text{CMZ}}$  and all gas is moving on circular orbits initially, the total angular momentum in the affected region is  $M_{\text{out}} v_{\text{circ}} R_{\text{out}}/2$ , therefore the gas circularizes at a mean radius of  $R_{\text{out}}/2$ . If the whole CMZ was affected, the circularization radius is 100 pc. Furthermore, gas that was initially outside and inside the circularization radius moves inward and outward, respectively, increasing the density contrast between the gas collected at the circularization radius and gas outside of it. This effect can turn an initially radially widespread gas distribution into a narrow ring.

The background density outside the sphere of influence of Sgr A\*, assuming a singular isothermal sphere potential, is

$$\rho_{\text{SIS}} = \frac{\sigma^2}{2\pi G R^2} \simeq 2.5 \times 10^{-21} \sigma_{100}^2 R_{100}^{-2} \text{ g cm}^{-3}, \quad (3)$$

which, assuming fully ionised gas of Solar metallicity ( $\mu = 0.63$ ), gives

$$n_{\text{SIS}} \simeq 2.5 \times 10^3 \sigma_{100}^2 R_{100}^{-2} \text{ cm}^{-3}. \quad (4)$$

The mean gas density within the CMZ, again assuming an  $R^{-2}$  density profile, is  $\rho_{\text{CMZ}} \sim 10^{-21} M_8 R_{100}^{-2} \text{ g cm}^{-3} \simeq 0.4 \rho_{\text{SIS}}$ . When the perturbed gas begins circularizing at around  $R_{\text{CMZ}}/2$ , it can easily pass the  $\rho_{\text{SIS}}$  threshold and become self-gravitating.

Gravitational instabilities can lead to formation of filaments and clumps of gas, as well as star clusters. This is a stochastic process, so I turn to numerical simulations to investigate the properties of the structures forming in a perturbed CMZ.

## 3 NUMERICAL MODEL

I run SPH simulations of the CMZ affected by a burst of AGN activity. The code used is GADGET-3, an updated version of the publicly available GADGET-2 (Springel 2005). It is a hybrid N-body/SPH code with individual particle timesteps and adaptive smoothing.

With these simulations, I intend to show how AGN activity can create an asymmetric distribution of gas and star clusters from initially smooth and regular conditions. Therefore, I set up the CMZ as a smooth disc with total mass  $M = 10^8 M_{\odot}$ , extending from an inner radius  $r_{\text{in}} = 5$  pc to outer radius  $r_{\text{out}} = 200$  pc, with a radial density profile  $\rho \propto r^{-2}$ . The CMZ has a constant rotational velocity  $v_{\phi} = 141$  km/s, which makes it rotationally supported against the gravity of the background potential. The disc gas is initialized with a constant temperature  $T = 3.2 \times 10^4$  K, giving a constant  $H/R = 0.25$ , i.e. the scale height of the disc is 50 pc from the midplane at the outer edge. In the vertical direction, the gas density decreases exponentially away from the midplane. This set up results in a surface density  $\Sigma \simeq 1.5 \times 10^4 (r/r_{\text{in}})^{-1} M_{\odot} \text{ pc}^{-2}$  and a radius-independent Toomre Q parameter  $Q \simeq 2.5$ . Thus the disc is initially marginally stable against axisymmetric perturbations and self-gravity.

The CMZ has  $N_{\text{cmz}} = 5 \times 10^5$  particles, giving a particle mass  $m_{\text{SPH}} = 200 M_{\odot}$  and mass resolution  $m_{\text{res}} = 40 m_{\text{sph}} = 8000 M_{\odot}$ . This is fine enough to resolve large molecular clouds and clusters. The spatial resolution is varying due to the nature of SPH. In the initial disc, it ranges from  $\sim 1$  pc at the inner edge to  $\sim 13$  pc at the outer edge; in the densest regions, the spatial resolution goes down to the minimum allowed smoothing length of 0.01 pc.

The disc is surrounded with a halo of diffuse ( $\rho_g = 10^{-3} \rho_{\text{SIS}}$ ) gas extending out to 5 kpc. Although a very crude approximation, this density approximately corresponds to the observed gas density in the Milky Way (Kalberla & Dedes 2008). The halo gas temperature is set at  $T_h = 2.4 \times 10^5$  K, equal to the virial temperature of the surrounding static, spherically symmetric isothermal background potential with velocity dispersion  $\sigma = 100$  km/s. I comment on the effects of the assumption of spherical symmetry in Section 5.1.

A SMBH with mass  $M_{\text{BH}} = 4.3 \times 10^6 M_{\odot}$  is embedded in the centre of the gas distribution. The sphere of influence of the SMBH extends only to  $R_{\text{infl}} \sim 1$  pc, therefore the SMBH gravity does not affect the dynamics of the gas. At the start of each simulation, the SMBH is turned on as an AGN of luminosity  $L = l L_{\text{Edd}}$  and radiates at this luminosity for a time  $t_q$ , after which the luminosity drops to zero. The AGN effect on the gas is modelled in two ways. First of all, the simulation employs a heating-cooling function appropriate for optically thin gas of Solar metallicity exposed to quasar radiation (Sazonov et al. 2005), with a temperature floor of  $T_{\text{floor}} = 10^4$  K. Secondly, AGN wind feedback is modelled with the help of virtual particles (Nayakshin et al. 2009). These particles are emitted by the SMBH every timestep. They have only trace mass, but carry momentum  $p_{\text{virt}} = k m_{\text{SPH}} \sigma$  each, where  $k = 0.1$  is an arbitrary constant, and energy  $E_{\text{virt}} = p_{\text{virt}} c/2$ ;  $p_{\text{virt}}$  also sets the number of virtual particles emitted each timestep. They move at a constant velocity  $v_w = 0.1c$  radially outward from the source. Whenever an SPH particle contains a virtual particle within its smoothing kernel, interaction between the two begins. The virtual particle gives up a fraction of its momentum and energy to the surrounding SPH particles, weighted by the SPH particles' smoothing kernel. The fraction given up in each interaction is set so that it takes  $\sim 10$  steps for each virtual particle to lose 99% of

Model ID	$l$	$t_q$ (Myr)	$t_{\text{sink}}$ (Myr)	$\langle \dot{M}_{\text{sink}} \rangle$ ( $M_{\odot} \text{ yr}^{-1}$ )	$M_{\text{sink,tot}}$ ( $10^6 M_{\odot}$ )	$a/b$
Control	—	0	—	0	0	—
Base1	1	1	4.5	15.0	26.7	1.39
Base2	1	1	4.6	11.3	27.6	1.34
Base3	1	1	—	4.9	29.7	1.53
Base4	1	1	3.4	12.7	37.8	1.39
Base5	1	1	4.0	14.2	37.8	1.43
Short1	1	0.7	2.6	11.8	28.1	1.43
Short2	1	0.7	3.0	13.6	28.9	1.27
Short3	1	0.7	3.5	13.2	24.3	1.55
Short4	1	0.7	3.0	13.2	27.9	1.38
L0.3	0.3	1	—	1.7	10.2	1.16
T0.3	1	0.3	1.4	3.7	23.0	1.09
T1.5	1	1.5	—	2.1	12.6	6.78*
L0.667T1.5	0.667	1.5	—	2.2	12.9	4.23*

**Table 1.** Parameters of the numerical models and most important results. The first column shows the model ID. The next two columns give the parameters: the AGN Eddington ratio,  $l \equiv L/L_{\text{Edd}}$ , and the duration of AGN phase in Myr,  $t_q$ . The final five columns are the primary results: time of onset of significant fragmentation (see text), mean fragmentation rate after the onset, total sink particle mass at  $t = 6$  Myr, CMZ ring major-to-minor axis ratio at  $t = 6$  Myr. Models Base1 to Base5 and models Short1 to Short5 differ in initial microscopic particle distribution, but have identical parameters. Numbers labelled with \* use a lower density threshold to identify the ring due to lack of significant structures.

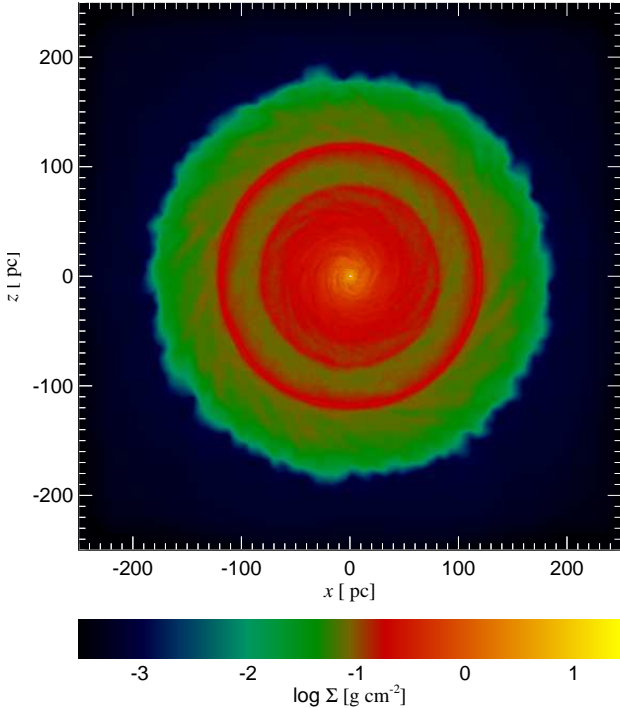


**Figure 1.** Projected gas density of the Control simulation at  $t = 6$  Myr. Several spiral patterns form in the disc, but there is no collapse or fragmentation.

its momentum/energy, at which point it is removed from the simulation. This method of transferring feedback self-consistently accounts for different optical depth of gas in different directions and enables the formation of anisotropic feedback-inflated bubbles. In all simulations presented here,

the wind shock is assumed to be adiabatic, therefore all of the wind kinetic energy  $L_w = 0.05 L_{\text{AGN}}$  is transferred to the gas.

In order to speed up the simulations and for easier tracking of the star formation process, we convert gas particles into sink particles according to a Jeans' condition. Whenever a gas particle density increases above the critical value

$$\rho_J = \left( \frac{\pi k_B T}{\mu m_p G} \right)^3 m_{\text{sph}}^{-2} \simeq 1.5 \times 10^{-12} T_4^3 \text{ g cm}^{-3}, \quad (5)$$

$$n_J \simeq 1.4 \times 10^{12} T_4^3 \text{ cm}^{-3}, \quad (6)$$

where  $T_4 \equiv T/10^4 \text{ K}$ , it is converted into a sink particle of the same mass, which subsequently interacts with the other particles only via gravity and can accrete other gas or sink particles once they come within  $10^{-4} \text{ pc}$ . The critical density is such that the corresponding Jeans' mass is equal to  $m_{\text{SPH}}$ . In all simulations, most gas particles stay well below the density threshold, with density increasing significantly only in self-gravitating clumps on sub-parsec scales; reducing the threshold by several orders of magnitude does not significantly affect the results.

There are fourteen simulations in total; their parameters -  $l$  and  $t_q$  - and main results are given in Table 1. I run one Control simulation with no AGN activity, in order to check whether the initial gas distribution is stable to its own self-gravity without external perturbations. Five simulations (Base1 to Base5) have identical parameters, but use stochastically different initial conditions, as the particles comprising the CMZ were cut from different parts of a relaxed glass distribution. The choice of  $l = 1$  and  $t_q = 1$  Myr is motivated by previous work (Zubovas & Nayakshin 2012), where we found that these parameters produce hot gas cavities very similar to the observed *Fermi* bubbles. Four more simulations (Short1 to Short4) also differ only in microscopic particle distribution and have  $t_q = 0.7$  Myr; this choice is motivated by the results of the Base simulations, as described

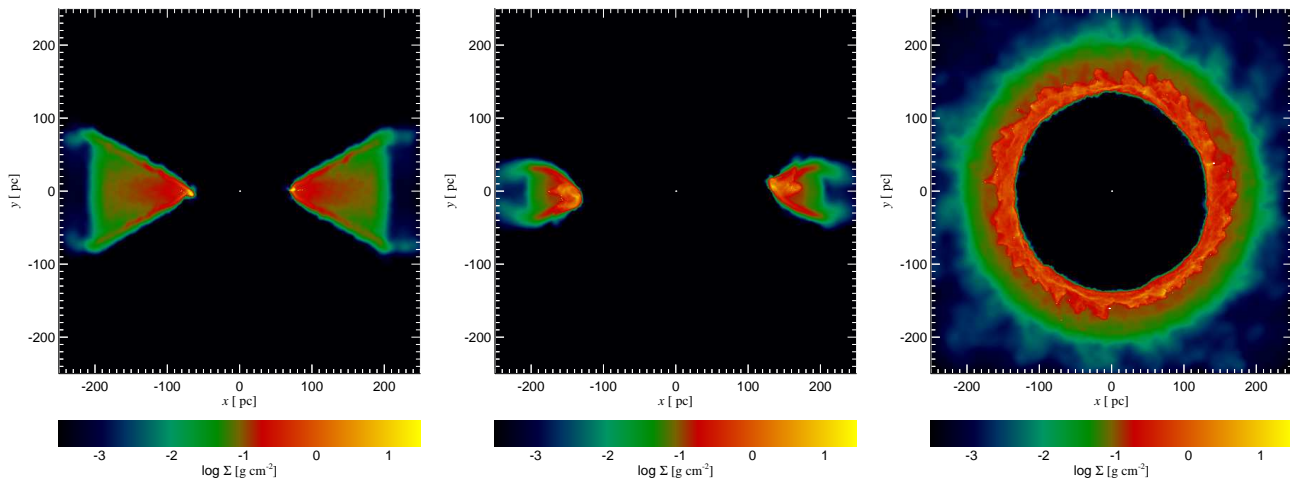


**Figure 2.** Projected gas density of fiducial run Base1 at early times. **Left:** cut side view at  $t = 0.5$  Myr, showing the radial structure of the CMZ disc. The central regions are pushed together and begin collapsing vertically, exposing parts of the disc further out to AGN feedback. **Middle:** cut side view at  $t = t_q = 1$  Myr. The whole disc is affected, with dense and thick inner ring and surface layers pushing into the outer parts. **Right:** top view at  $t = t_q = 1$  Myr. A transition region is visible, with spiral perturbations and self-gravitating clumps.

below. The final four simulations show the effects of varying  $l$  and  $t_q$  further, as these parameters are least constrained by observations and current models. All but one of these four simulations use the same initial conditions as the Base1 and Short1 models; one simulation, L0.3, crashes before finishing due to one sink particle growing to a mass greater than that of Sgr A\*, so I reran it with initial conditions identical to those of model Base2. All simulations ran for 6 Myr, the presumed time interval since the start of the AGN phase.

## 4 RESULTS

I first present the results of the Control simulation, which has no AGN activity and is designed to show the stability of the initial gas configuration. Then I present the five Base models, which all have the same AGN parameters: an Eddington-limited outburst lasting for  $t_q = 1$  Myr. I discuss the morphology and the structures forming in the perturbed CMZ, derive fragmentation rates and properties of the major sink particle clusters. Later, I comment on the effect of varying the AGN outburst duration and luminosity.

### 4.1 Control simulation

In this simulation, the gas disc is allowed to evolve freely without external perturbation. Soon after the start of the simulation, a circular overdensity forms in the centre of the ring and moves outward with velocity  $v \sim 40$  km/s; it reaches the outer edge of the disc at  $t \simeq 4$  Myr, at which point the disc radius has shrunk to  $\simeq 160$  pc. This happens because the initial conditions feature sharp density cutoffs at both the inner and outer edge. As the disc relaxes, density waves form, but the one on the outer disc is much weaker due to the lower density contrast.

Subsequently, starting from  $\sim 1$  Myr after the start of the simulation, spiral density perturbations form in the inner

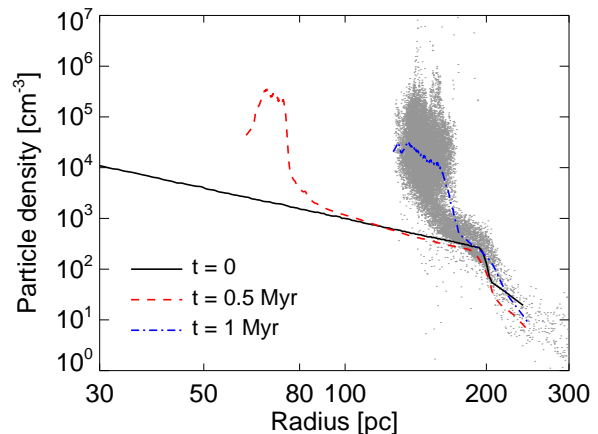


**Figure 3.** Radial density profiles of CMZ gas in the model Base1 at  $t = 0$  (black),  $t = 0.5$  Myr (red) and  $t = 1$  Myr (blue). Grey points are a sample of SPH particle densities at  $t = 1$  Myr.

part of the disc. By  $t = 6$  Myr, they are present throughout the disc, with a stronger density contrast in the inner  $\simeq 80$  pc, reflecting the shorter dynamical timescale there. The formation of spiral density waves is expected, since the Toomre  $Q$  factor of the initial configuration is 2.5, around the limit where it becomes unstable to such perturbations ( $Q < 2$ ).

Figure 1 shows the projected gas density map of the disc at  $t = 6$  Myr. Despite the presence of both circular and spiral density waves, no fragmentation has occurred in the CMZ, and no sink particles formed. This lack of fragmentation happens partially due to the imposed temperature floor of  $10^4$  K; if the gas could cool down to much lower temperatures, some fragmentation would be expected. However, stellar feedback and external radiation might keep the

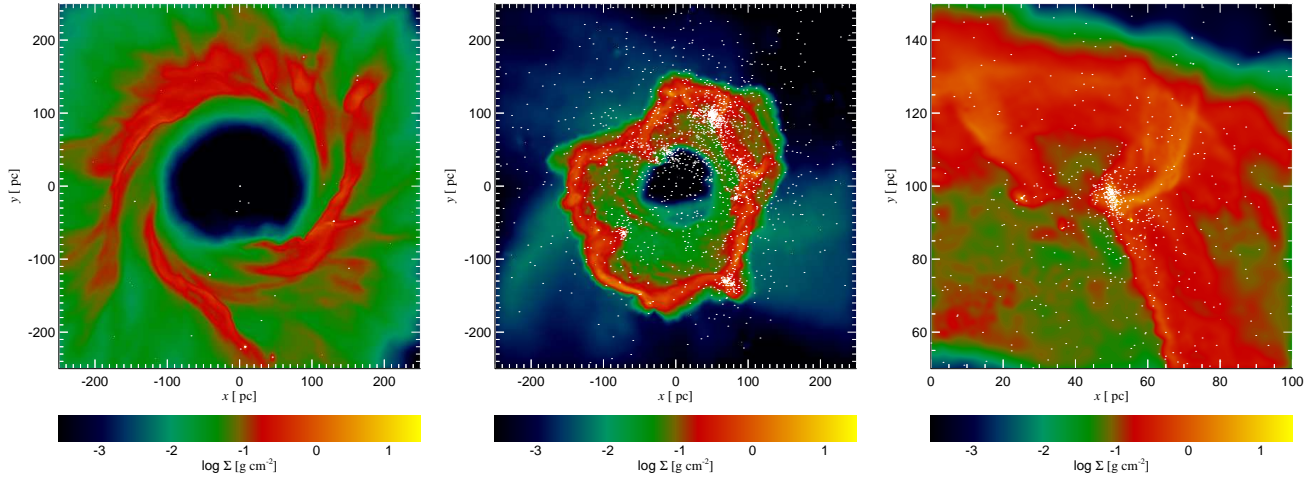


**Figure 4.** Projected gas density of fiducial run Base1 after the AGN switches off. All images show top view. **Left:**  $t = 3$  Myr; spiral perturbations are falling inward and facilitating radial migration of CMZ gas. **Middle:**  $t = 6$  Myr; a narrow asymmetric ring of gas is winding around the Galactic centre. White dots show the sink particles; several clusters can be identified. **Right:** A zoom-in on the most massive sink particle cluster.

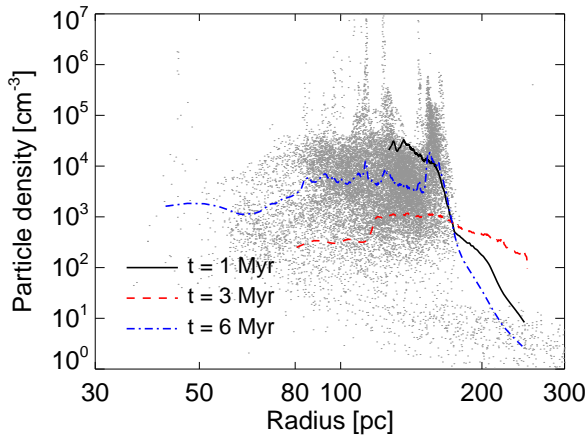


**Figure 5.** Radial density profiles of CMZ gas in the model Base1 at  $t = 1$  Myr (black),  $t = 3$  Myr (red) and  $t = 6$  Myr (blue). Grey points are a sample of SPH particle densities at  $t = 6$  Myr.

gas in this configuration above the temperature required for fragmentation. I discuss the importance of the gas equation of state in Section 5.5.1.

## 4.2 Fiducial runs: $l = 1$ , $t_q = 1$ Myr

### 4.2.1 Feedback-driven expansion

From the start of the simulation, AGN wind impacts the inner edge of the CMZ disc and pushes it outward. The expansion velocity is initially approximately constant,  $v_{r,\text{out}} \simeq 150$  km/s  $= \sqrt{2}\sigma$ . Formally, the purely energy-driven velocity of expansion should be  $\sim 330$  km/s, while purely momentum-driven velocity should be  $\sim 25$  km/s. The actual velocity is in between the two, suggesting that a large fraction ( $\sim 80\%$ ) of the energy is reflected away from the dense gas and works to form bubbles in the diffuse halo (this effect

was investigated in more detail by Zubovas & Nayakshin 2014). Gas temperature at the edges of the CMZ increases to  $> 10^5$  K, resulting in some gas evaporating from the surfaces and escaping into the diffuse halo; meanwhile, most of the gas stays close to the temperature floor. After  $\sim 0.5$  Myr (Figure 2, left panel) gas in the inner parts of the CMZ is compacted so much that vertical gravitational collapse begins, as the Toomre  $Q$  parameter in that region drops to  $< 1$ . The inner parts of the disc become thinner and less exposed to the AGN wind (red line in Figure 3); meanwhile, parts further away become more exposed and start moving radially outward. Globally, this results in a transition region forming between the evacuated inner part of the disc and the stable outer parts. A surface layer of higher density forms in the outer part of the disc, where the disc gas is pushed inward by the expanding hot bubble in the halo (Figure 2, middle panel).

By the end of the AGN outburst, i.e. at  $t = 1$  Myr, the transition region extends from  $\sim 130$  to  $\sim 160$  pc (Figure 2, right panel; also blue line and grey points in Figure 3). Column densities in the transition region exceed  $1 \text{ g cm}^{-2}$ ; this is enough to bring the Toomre  $Q$  parameter below 1 ( $\Sigma_{\text{crit}} \simeq 0.4 R_{100}^{-1} \text{ g cm}^{-2} \simeq 1700 R_{100}^{-1} M_{\odot} \text{ pc}^{-2}$ ). As a result, spiral perturbations and self-gravitating clumps form within the transition region.

All five Base models evolve very similarly during this stage, since their evolution is dominated by a global process (AGN feedback), rather than local gravity.

### 4.2.2 Fragmentation

Once AGN activity ends, the CMZ material collapses back toward the centre. The circularization radius is  $\sim 60$  pc, but falling material overshoots this limit and moves to radial distances of  $\sim 40$  pc before expanding again. In effect, individual gas particles move on eccentric orbits and the whole disc appears to breathe. The particles on the outer edge of the transition region at  $t = 1$  Myr continue moving outward



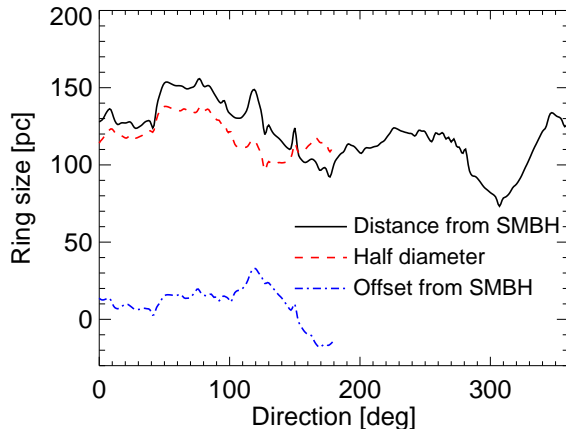


**Figure 6.** Average radius (black solid line), half-diameter (red dashed line) and displacement (blue dot-dashed line) of the dense gas ring, defined as  $n > 100 \text{ cm}^{-3}$ , as function of direction counterclockwise from left in model Base1 at  $t = 6 \text{ Myr}$ . Gas further than 200 pc from the centre was excluded when calculating these values. The radius (i.e. distance from the origin to the dense ring) varies between  $\sim 80$  and  $\sim 150 \text{ pc}$ . The half-diameter (half the distance between the ring on opposite sides of the origin) varies between  $\sim 100$  and  $\sim 140 \text{ pc}$ , and the SMBH is displaced from the centre of the ring by about 20 pc.

for a while, encompassing the whole disc and causing it to expand to a maximum radius of  $\sim 270 \text{ pc}$  at  $t = 2 \text{ Myr}$ .

During this time, spiral perturbations continue to grow in the disc. By  $t = 2 \text{ Myr}$ , they are clearly visible. By  $t = 3 \text{ Myr}$ , they have become significant density enhancements, facilitating infall of material to small radii (Figure 4, left panel). The formation and growth of perturbations is a stochastic process, and as a result, differences among the five Base models begin to manifest. In the rest of this subsection, the descriptions refer to model Base1, unless otherwise noted.

By the end of the simulation, the CMZ gas is distributed strongly anisotropically, with a narrow ( $d_{\text{ring}} \sim 20 - 40 \text{ pc}$ ) ring winding around the Galactic centre at distances ranging from  $r_{\text{min}} \sim 80 \text{ pc}$  to  $\sim 150 \text{ pc}$  (top-left and bottom in the middle panel of Figure 4, respectively; see also Figures 5 and 6). The ring has a sharp outer edge, with density dropping by several orders of magnitude outside  $\sim 150 \text{ pc}$ , and a less pronounced inner edge where density decreases by approximately a factor 4. The ring can be roughly approximated as an ellipse with semimajor axis of 140 pc and semiminor axis of 100 pc, with the semimajor axis making a  $30^\circ$  angle with the Y axis. The SMBH is displaced by  $\sim 20 \text{ pc}$  from the geometric centre of the ellipse. The total mass of the gas ring, defined as having gas with density  $n_{\text{dense}} > 100 \text{ cm}^{-3}$ , is  $M_{\text{dense}} = 6.9 \times 10^7 M_\odot$ . This value does not include the mass of sink particles (see below). The cutoff density is chosen in such a way that if the selected gas cools down isobarically to 20 K, the column density through the ring would be  $N_{\text{dense}} \simeq n_{\text{dense}} \times (T_{\text{floor}}/20\text{K})^{2/3} \times d_{\text{ring}} \simeq 4 \times 10^{23} \text{ cm}^{-2}$ , equal to the threshold used when identifying the ring from infrared observations (Molinari et al. 2011).

The densest parts of the perturbations become self-gravitating clumps and create sink particles. The first sink

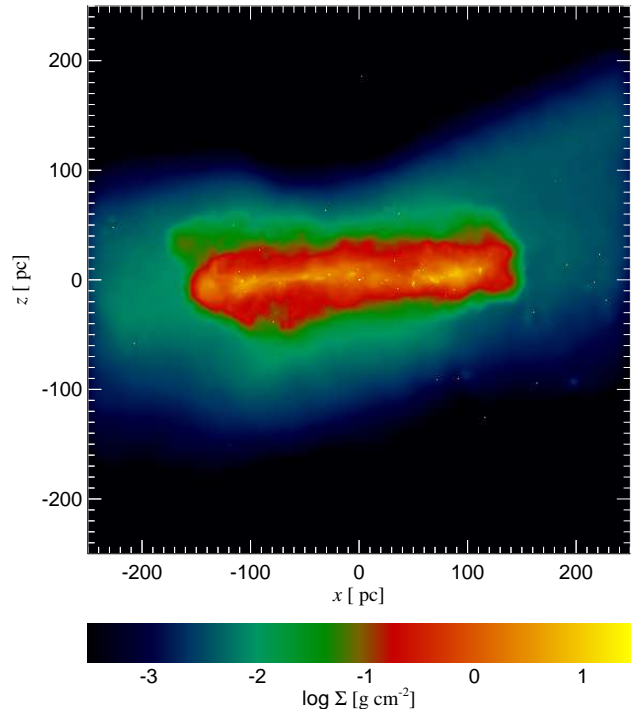


**Figure 7.** Side view of model Base1 at  $t = 6 \text{ Myr}$ . The gas ring is slightly disturbed, but generally stays on the  $Z = 0$  plane.

particles appear before the AGN switches off, but fragmentation starts in earnest at  $t \gtrsim 4.5 \text{ Myr}$ . There are five regions of intense fragmentation, lighting up one after another. In addition, some sink particles form in the dense filaments; these most likely represent small star clusters and associations with masses at or below the simulation resolution of  $8000 M_\odot$ . By the end of the simulation, the total mass in sink particles is  $M_{\text{sink}} = 2.8 \times 10^7 M_\odot$ . Thus the total mass in sink particles and dense gas is  $\sim 9.7 \times 10^7 M_\odot$ , i.e. almost all of the initial CMZ material ends up either converted into sink particles or in the dense gas ring. The presence of dense gas is not unexpected, since the initial conditions contain gas denser than the threshold used to identify the ring; however, the transformation from a smooth disc into a narrow ring is remarkable. The average fragmentation rate over the 1.5 Myr period of intense fragmentation is  $\dot{M}_{\text{frag}} \simeq 15 M_\odot \text{ yr}^{-1}$ , but it can rise up to  $\sim 25 M_\odot \text{ yr}^{-1}$  (see Figure 9). Assuming a typical star formation efficiency on such mass scales of 2–10% gives a star formation rate  $\dot{M}_* \simeq 0.25 - 1.25 M_\odot \text{ yr}^{-1}$ , dropping below  $0.2 M_\odot \text{ yr}^{-1}$  at  $t = t_n = 6 \text{ Myr}$ .

Most sink particles move far away from the regions where they form; this is most likely a numerical effect arising due to the timesteps and smoothing lengths of the sink particles being too large for proper orbit integration within the clusters. However, one can still identify five or six clusters (Figure 4, middle panel), distributed asymmetrically within the CMZ. The most massive such cluster is located at  $\{X, Y\} \simeq \{50, 100\} \text{ pc}$  (visual estimate; Figure 4, right panel). By measuring the cumulative mass within a given distance from the centre of the cluster, I estimate its size

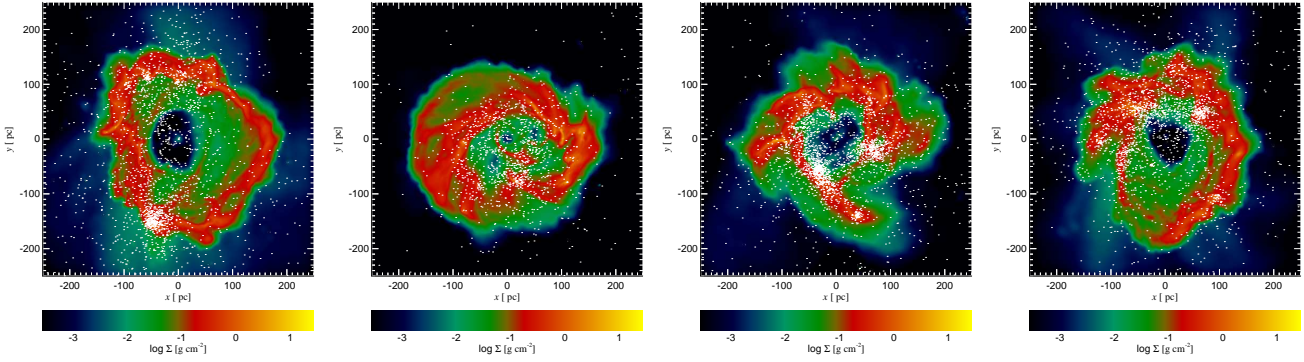


**Figure 8.** Projected gas column density of models Base2 (left panel), Base3 (second panel), Base4 (third panel) and Base5 (last panel) at  $t = 6$  Myr. The gas morphologies differ significantly, with no well-defined rings in any of the models.

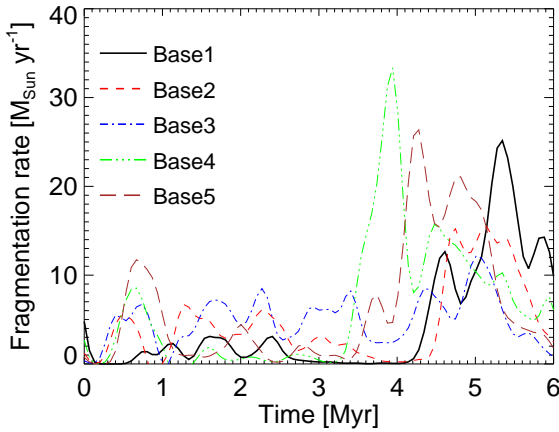


**Figure 9.** Fragmentation rates in the five Base models. The algorithm calculates the change in total sink particle mass, so the actual rates may be slightly higher if many sink particles are accreted by the central SMBH. All models except Base3 show qualitatively similar behaviour - initially small fragmentation rates lead to a surge once the CMZ ring begins fragmenting in earnest, at 3.5 – 4.5 Myr. In the Base3 model, fragmentation rates stay roughly the same throughout the simulation.

to be  $R_{c1} \sim 10$  pc and mass  $2.8 \times 10^6 M_\odot$ . A more rigorous estimate of cluster size is not reasonable due to lack of numerical resolution and appropriate star formation physics within the model. Other clusters have sizes  $\sim 5$  pc or less and masses  $\sim 0.7 - 1.6 \times 10^6 M_\odot$ . The typical star formation efficiency leads to star cluster mass estimates of  $1.4 \times 10^4 - 2.8 \times 10^5 M_\odot$ , very similar to the masses of the observed clusters. The orbits of the sink particle clusters, much like the gas orbits, are non-circular and may be strongly irregular. This is consistent with observations of the motion of both Arches (Stolte et al. 2008) and Quintuplet (Stolte et al. 2014) clusters.

The gas and sink particles are distributed almost symmetrically around the  $Z = 0$  plane. In Figure 7, I show the gas column density in a side view of the CMZ. Small variations in gas height and position are visible across the CMZ, but the displacement from  $Z = 0$  does not exceed the ring thickness  $h \lesssim 40$  pc.

The other four Base models exhibit very different gas morphologies in the XY plane. Figure 8 shows the gas distribution in those models at  $t = 6$  Myr. All four gas distributions are clumpy, but the large-scale gas distribution differs. Model Base2 (left panel) has a full ring, model Base5 (right panel) shows approximately two thirds of a ring with a large gap in the bottom-left direction, model Base4 has prominent spiral streamers which may coalesce into a ring structure in several Myr. Finally, model Base3 has a very weak (low density contrast) and highly off-centre elliptical structure, with very dense gas at the apocentre in the positive-X direction. It is interesting to note that even though the morphologies of the five models differ significantly, the formal ratio of semimajor to semiminor axis lengths, when defined as the maximum ratio of mean diameters of the dense gas features in two perpendicular directions, is rather similar, ranging from 1.34 to 1.53 (Table 1, last column).

The morphological differences are reflected in the fragmentation rates (Figure 9 and Table 1, columns 4-6). In models Base4 and Base5, several prominent bursts of fragmentation occur earlier than in Base1, starting at  $t \simeq 3.4 - 4.0$  Myr. The peak fragmentation rates in these models are slightly higher than those in Base1, while the mean rates over the significant fragmentation period are similar. In model Base2, significant fragmentation starts at a similar time as in Base1, but proceeds slower. In model Base3 the fragmentation rate stays approximately constant, between  $5 - 10 M_\odot \text{ yr}^{-1}$ , throughout the simulation. The total mass of sink particles varies from  $2.7 \times 10^7 M_\odot$  in Base1 and Base2 to  $3.8 \times 10^7 M_\odot$  in Base4 and Base5, with an average value  $(3.2 \pm 0.5) \times 10^7 M_\odot$ . The vertical structure of all four models is very similar to that of the Base1.

#### 4.2.3 Mixing of gas and angular momentum

A general outcome of the five Base simulations is that an initially smooth and stable distribution of gas becomes clumpy and anisotropic. This can be understood as a consequence of mixing of gas and its angular momentum. During the AGN phase, a large amount of gas (almost the whole CMZ) is pushed together into a narrow ring. This both increases the surface density of this gas, making it prone to gravitational instabilities, and efficiently mixes the angular momentum of



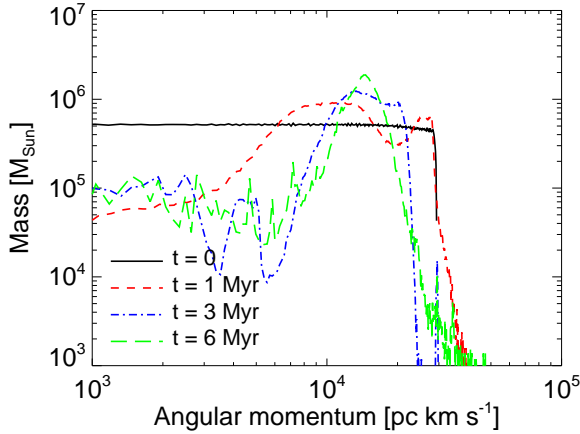


**Figure 10.** Distribution of CMZ gas angular momentum in the model Base1 at  $t = 0, 1.5, 3$  and  $6$  Myr (black solid, red dashed, blue dot-dashed and green long-dashed lines, respectively). The gas initially has a flat angular momentum distribution, which becomes progressively more squashed toward a single peak at  $l \sim 1.5 \times 10^4$  pc km/s.

gas, ensuring that the ring disperses slowly after the AGN switches off.

To show this, I plot the angular momentum distribution of gas at  $t = 0$ ,  $t = 1$  Myr (end of AGN phase),  $t = 3$  Myr and  $t = 6$  Myr in Figure 10. Initially, the angular momentum distribution is flat throughout the disc, since each annulus contains the same mass of material. AGN feedback pushes gas with low angular momentum (central parts of the disc) to merge with the high angular momentum gas, leading to a bump at middle values  $l \sim 10^4$  pc km/s; the outer edge of the disc is not perturbed radially at  $t = 1$  Myr. Later, this process continues, and by  $t = 3$  Myr, the bump has moved to larger values due to mixing with the material at the outskirts of the disc. Even by the end of the simulation, material is still being pushed together by spiral perturbations and gravitational instabilities; there is, however, a growing high angular momentum tail, which arises due to viscous spreading of the ring material. The total mass of material with very low angular momentum increases after the AGN switches off; this represents clumps of gas falling inward and coming very close to the SMBH, potentially feeding it (see Section 5.4).

#### 4.3 Shorter AGN episode models: $t_q = 0.7$ Myr

The five Base models consistently produce gas rings, or parts of rings, that are too large and form sink particle clusters too late as compared with observations of the CMZ structure. Motivated by this, I run four models with  $t_q = 0.7$  Myr, labelled Short1 to Short4 (see Table 1 for details and main results). As before, the models have stochastically different initial conditions, leading to different fragmentation histories and gas morphologies at the end of the simulation.

Qualitatively, the evolution of the Short models is very similar to that of the Base models. Initially, the AGN wind pushes disc gas together into a narrow ring, which becomes gravitationally unstable and fragments over several dynamical

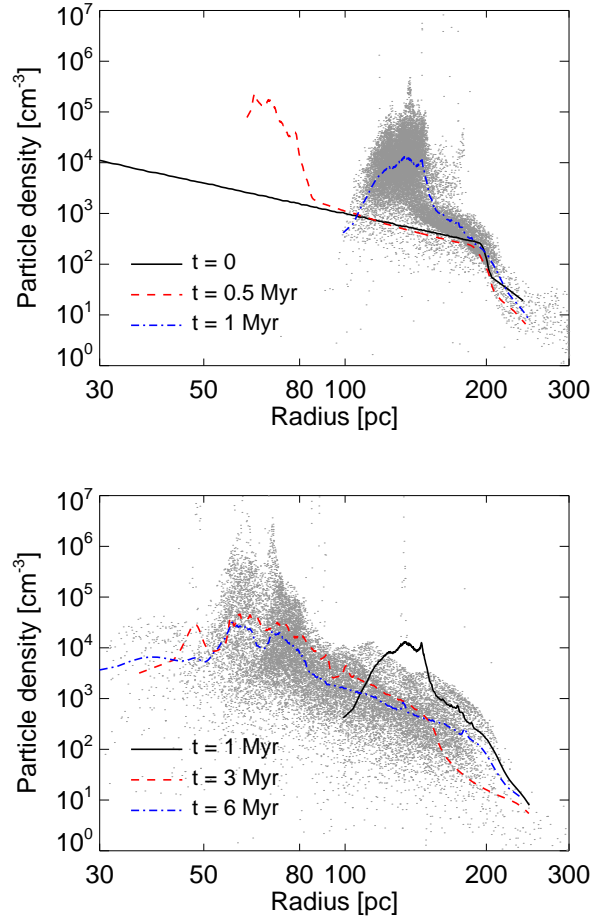


**Figure 12.** Radial density profiles of CMZ gas in model Short1. **Top panel:**  $t = 0$  (black solid),  $t = 0.5$  Myr (red dashed) and  $t = 1$  Myr (blue dot-dashed). Grey points are a sample of SPH particle densities at  $t = 1$  Myr. **Bottom panel:**  $t = 1$  Myr (black solid),  $t = 3$  Myr (red dashed) and  $t = 6$  Myr (blue dot-dashed). Grey points are a sample of SPH particle densities at  $t = 6$  Myr.

ical times. The shorter AGN episode duration results in a smaller initial extent of the ring, which is mirrored by the final sizes as well (see Figures 11, 12 and 13). The ring eventually has a radial extent from  $\sim 50$  to  $\sim 80$  pc from the centre, comparable to the observed CMZ size. The density contrast on each edge is not as sharp as in the Base models, but still noticeable, so that the ring can be identified as such (Figure 12, blue dashed line and points in the bottom panel). The ring evolves faster: since the expansion of the ring happens at constant velocity, and the subsequent evolution depends on the dynamical time, which increases linearly with radius, one would expect  $t_{\text{frag,short}}/t_{\text{frag,base}} = t_{q,\text{short}}/t_{q,\text{base}} = 0.7$ . In fact, rapid fragmentation begins  $2.5 - 3$  Myr after the start of the simulation (Figure 14), almost 30% earlier than in the Base models, validating this simple explanation. The star clusters forming during this period would have ages consistent with observations of the Arches and Quintuplet clusters. Significant fragmentation has finished in all models by 6 Myr, so the expected star formation rate today is  $< 0.2 M_\odot \text{ yr}^{-1}$ . The masses and sizes of the star clusters are more difficult to determine than in the Base models, since

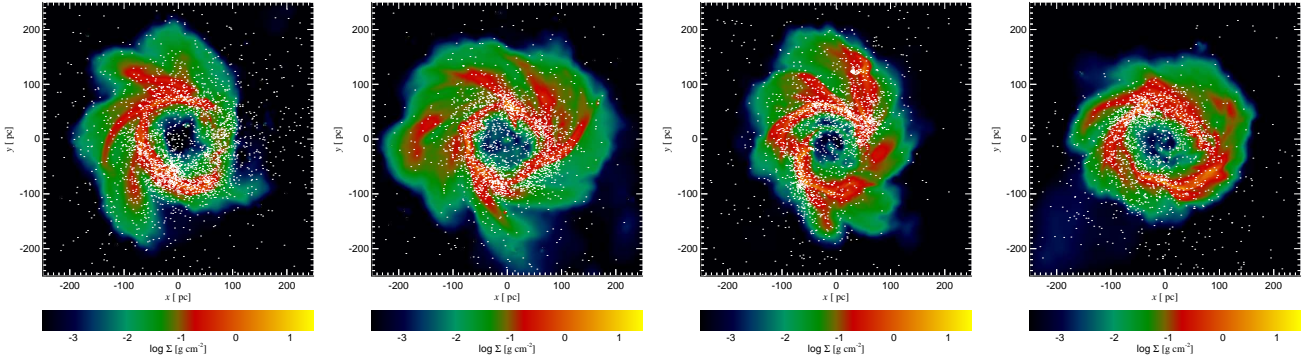


**Figure 11.** Projected gas column density of models Short1 (left panel), Short2 (second panel), Short3 (third panel) and Short4 (last panel) at  $t = 6$  Myr. The perturbed gas rings are smaller than in the Base models, with a variety of structures present.

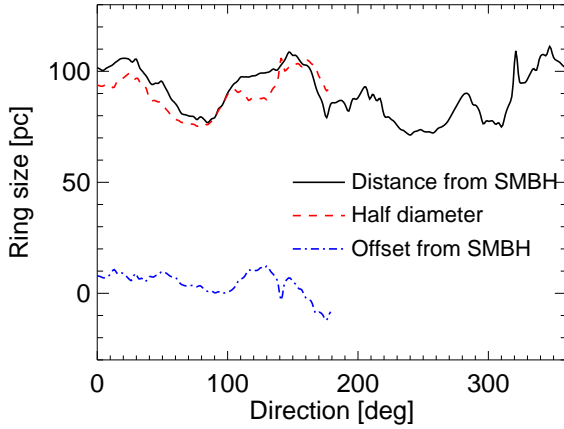


**Figure 13.** Average radius (black solid line), half-diameter (red dashed line) and displacement (blue dot-dashed line) of the dense gas ring, defined as  $n > 100 \text{ cm}^{-3}$ , as function of direction counterclockwise from left in model Short4 at  $t = 6$  Myr. The radius varies between  $\sim 70$  and  $\sim 110$  pc. The half-diameter varies between  $\sim 75$  and  $\sim 105$  pc, and the SMBH is displaced from the centre of the ring by about 10 pc.

the older sink particle clusters have lost more members due to numerical effects. The total masses of sink particles forming in the four simulations are  $2.4\text{--}2.9 \times 10^7 M_\odot$ , only slightly lower than in the Base models.

The final shape of the gas rings varies among the four Short models (Figure 11), but the rings are generally more regular than in the Base simulations. Their ellipticity is similar to the longer-duration runs,  $a/b = 1.27\text{--}1.55$  (Table 1, last column), but the displacement of the SMBH from the centre generally does not exceed 10 pc. As an example, I plot the radius, half-diameter and displacement of the gas ring in the Short4 model in Figure 13. The ring half-diameter varies between 75 and 105 pc, quite similar to the 60 and 100 pc of the model by Molinari et al. (2011). Sgr A\* is displaced from the centre of the ring by  $\sim 10$  pc, less than in the Molinari et al. (2011) model, but that value is less strongly constrained than the size of the ring itself.

Overall, the Short models give a final gas distribution in better agreement with the observed shape and size of the

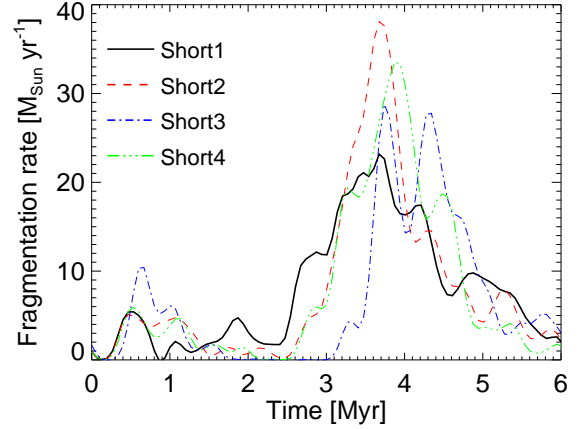


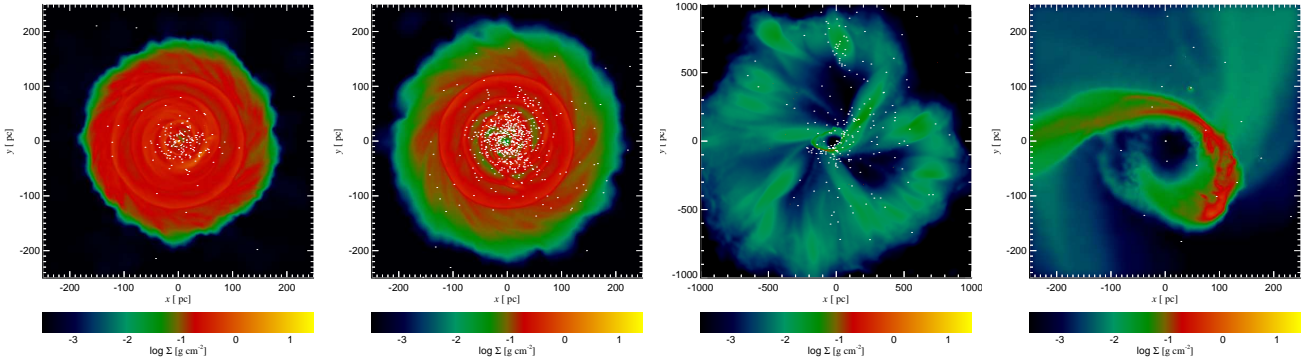
**Figure 14.** Gas fragmentation rate as function of time in the four Short models. The bursts of significant fragmentation occur at  $t = 2.5\text{--}3$  Myr, earlier than in the Base models.

CMZ than the Base models. However, the stochastic evolution of the gas ring results in large uncertainties regarding various more detailed parameters (such as the number, size and mass of star forming regions and young clusters), preventing a more rigorous constraint on past AGN activity from being made. I now turn to the four models designed to show the effect of varying the AGN duration and luminosity more significantly.

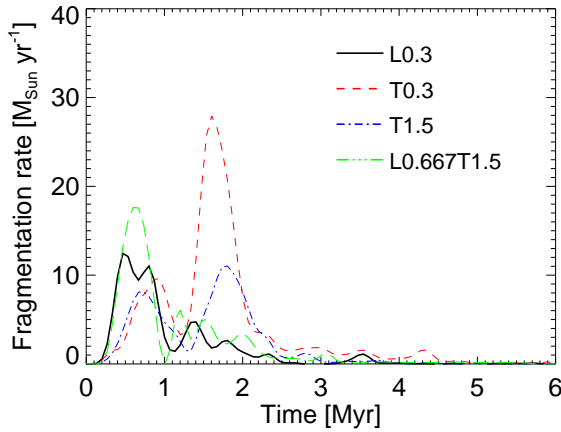
#### 4.4 Parameter variation

Figure 15 presents the gas and sink particle morphology of the final four models with varying parameters. From left to right, these models are: L0.3, where the AGN luminosity is decreased to  $0.3L_{\text{Edd}}$ , T0.3, where  $t_q = 0.3$  Myr, T1.5, where  $t_q = 1.5$  Myr, and L0.667T1.5, which has both  $L = 0.667L_{\text{Edd}}$  and  $t_q = 1.5$  Myr.

Both L0.3 and T0.3 models show similar morphology. The time evolution of the models is also similar - a short or weak burst of AGN activity only affects a small inner part of the CMZ before switching off. The disturbance propagates outwards, but grows progressively weaker and is unable to



**Figure 15.** Gas column density of models L0.3 (left panel), T0.3 (second panel), T1.5 (third panel) and L0.667T1.5 (last panel) at  $t = 6$  Myr. The gas morphologies differ significantly, with various structures visible. Note the different scale in the third panel.



**Figure 16.** Fragmentation rate in models L0.3 (black solid line), T0.3 (red dashed), T1.5 (blue dot-dashed) and L0.667T1.5 (green long-dashed). In all models, fragmentation is stronger soon after, or even during, the AGN phase, gradually decreasing with time as the gas distribution relaxes.

produce gravitational instability in the outer parts of the CMZ. Some clumps form in the central regions; they produce sink particles and create spiral waves, which affect the whole disc and are clearly visible in the morphology plots. The T0.3 model produces more sink particles (total mass at  $t = 6$  Myr is  $M_{T0.3} = 2.3 \times 10^7 M_\odot$  and  $M_{L0.3} = 1.0 \times 10^7 M_\odot$ ), but in both models, essentially all fragmentation occurs at  $t < 2$  Myr (see Figure 16, black solid and red dashed lines). It is interesting that model T0.3 has a single burst of fragmentation at  $t \simeq 1.6$  Myr, which occurs when the perturbed material falls back to the centre of the disc and reaches highest density.

In model T1.5, the prolonged action of the AGN unbinds most of the CMZ gas and allows it to disperse over a very wide region (Figure 15, third panel; note that the physical scale is different than in the other two). This can be expected, because even though most of the outflow energy escapes in directions perpendicular to the CMZ, some of that energy is retained and adds to the pure momentum push in unbinding the gas disc. The gas density in the central regions is reduced and there is very little gravitational

fragmentation (Figure 16, blue dot-dashed line). Some spiral perturbations are present, and a ring of relatively dense gas forms at a distance  $d \sim 100$  pc from the centre, but this ring contains only  $\sim 5 \times 10^6 M_\odot$  of gas. Sink particles disperse throughout the volume, with roughly one third of the total  $M_{T1.5} = 1.3 \times 10^7 M_\odot$  escaping from the central 200 pc of the Galaxy.

The model L0.667T1.5 provides the same energy input to the CMZ as the Base models, but spread more gradually. Its evolution is markedly different from the Base models. A more gradual energy input results in a much lower density contrast in the CMZ, which then leads to more gas being expelled from the system and far less fragmentation (Figure 16, green triple-dot-dashed line). The total sink particle mass at  $t = 6$  Myr is  $M_{L0.667T1.5} = 1.3 \times 10^7 M_\odot$ . This mass is concentrated in just a few sink particles, which are distributed with no particular structure throughout the simulation volume (Figure 15, right panel).

All four models with parameter variation exhibit very little fragmentation after  $t = 2$  Myr, making the clusters formed in these simulations older than those observed in the Galactic Centre. In addition, the morphology of dense gas differs significantly from the observed ring. These discrepancies suggest that the set of parameters chosen for the Base and Short models - a 0.7 – 1 Myr long Eddington-limited burst of AGN activity 6 Myr ago - are the best fit to the Sgr A\* activity that could have produced the dense CMZ ring and massive star clusters.

#### 4.5 Summary of results

A brief summary of the main results of the simulations is as follows:

- A burst of Eddington-limited AGN feedback lasting for 0.7 – 1 Myr is able to transform an initially smooth gas disc in the Galactic centre into a clumpy asymmetric distribution.
- The morphology of the distribution depends strongly on stochastic processes - spiral and gravitational instabilities. It is not guaranteed, but seemingly quite likely, that an elliptical ring of dense gas forms in the CMZ, and that the major-to-minor axis ratio of the ring, as well as the ring size, is very similar to the observed one.

- Fragmentation of the CMZ into sink particles takes off several dynamical times after the AGN activity finishes. The dynamical time, and hence the age of the sink particle clusters, depends on the duration of the AGN episode. For the  $t_{rmq} = 1$  Myr episode, fragmentation occurs  $\sim 3.5\text{--}5.5$  Myr after the start of the simulation, i.e.  $0.5\text{--}2.5$  Myr ago. If the AGN episode lasts for only  $t_q = 0.7$  Myr, fragmentation starts earlier,  $3.5$  Myr ago. The average fragmentation rate during the last  $6$  Myr is  $< 10M_\odot \text{ yr}^{-1}$ , with peaks reaching  $\gtrsim 30M_\odot \text{ yr}^{-1}$ . Given a typical star formation efficiency on the mass scale of the sink particles,  $\epsilon_* = 2\text{--}10\%$ , the star formation rate in the CMZ is  $\dot{M}_* \lesssim 0.2\text{--}1M_\odot \text{ yr}^{-1}$ , with bursts up to  $\sim 3M_\odot \text{ yr}^{-1}$ . By  $t = 6$  Myr, fragmentation in the Short models has dropped to  $< 2M_\odot \text{ yr}^{-1}$ , corresponding to a star formation rate of  $< 0.2M_\odot \text{ yr}^{-1}$ ; however, fragmentation is still ongoing in some Base models.

- The mass of sink particles formed in the Base simulations is  $(2.7\text{--}3.8) \times 10^7 M_\odot$ , predominantly distributed in a few clumps, each with mass in the range  $(0.5\text{--}3) \times 10^6 M_\odot$ . Using the same star formation efficiency as above, the star clusters formed should have masses in the range  $10^4\text{--}3 \times 10^5 M_\odot$ . The Short simulations form a slightly smaller total mass of sink particles, but the cluster masses are more difficult to determine due to numerical effects.

- An AGN outburst that either has a lower luminosity,  $L = 0.3L_{\text{Edd}}$ , or a significantly shorter duration,  $t_q = 0.3$  Myr, produces a perturbation to the CMZ that is too weak to create a dense ring with embedded young star clusters. Conversely, a longer AGN burst duration,  $t_q = 1.5$  Myr, disrupts the CMZ, leaving only a minor fraction of the gas bound in the Galactic centre.

- An AGN outburst with the same total energy output as in the Base models, but spread on a longer timescale produces a weaker density contrast in the CMZ disc, which leads to an almost non-existent dense gas ring and far less sink particle formation. This type of outburst might still enhance the existing density contrasts in the CMZ, but is unable to shape it to the present state from smooth initial conditions.

## 5 DISCUSSION

### 5.1 Current properties of the CMZ

The numerical models presented here adequately explain the origin of some of the peculiar CMZ properties. Notably, an Eddington-limited AGN episode which started  $6$  Myr ago and lasted for  $0.7\text{--}1$  Myr could have shaped an initially axially symmetric CMZ disc into an elliptical, off-centre dense gas ring with embedded massive molecular clouds and star clusters. The total mass of dense gas and sink particles (which represent both stars and gas denser than resolvable in the simulation) is very similar to the observed value, although this is potentially an imprint of the initial conditions, and a more (less) massive initial gas disc would produce a more (less) massive dense gas ring at the end. The fact that such complex structures can be created from axisymmetric initial conditions suggests that lopsided nuclear structures should be a common feature of galaxies (see Section 5.3 below).

The rate of formation of new sink particles at the end of the simulation, when multiplied by the typical star formation efficiency, produces a star formation rate estimate similar to the observed value  $\sim 0.06\text{--}0.08M_\odot \text{ yr}^{-1}$ . This value is at first sight puzzling on two accounts. It is higher than could be expected from steady-state arguments (Zubovas et al. 2013), i.e. the current SFR would exhaust the molecular gas reservoir in much less than the age of the Galaxy. On the other hand, it is several orders of magnitude lower than expected from the surface density of the gas (Longmore et al. 2013). Explanations for the first mismatch include bar-induced inflow of material, which replenishes the gas content in the Galactic centre (Rodríguez-Fernández & Combes 2008), while the second can be explained by an unusually high level of turbulence in the Galactic centre molecular clouds, which reduces the star formation rate at a given surface density (Rathborne et al. 2014). The AGN-induced fragmentation model can explain both phenomena simultaneously. The elevated star formation rate is a transient phenomenon, caused by the AGN episode compressing the gas, and will likely drop by at least a factor of a few in the upcoming several Myr. Meanwhile, the molecular clouds forming from the fragmenting CMZ disc are subject to very high external pressure from the expanding AGN outflow (the *Fermi* bubbles; see Zubovas et al. 2013), which cause them to have higher density and turbulence (Elmegreen & Efremov 1997), leading to a higher SFR threshold (Longmore et al. 2013; Rathborne et al. 2014).

The AGN-induced fragmentation model naturally explains why the massive clusters in the CMZ are younger than the nuclear star cluster: the NSC formed from the gas that fed the AGN outburst, while the CMZ clusters formed from the perturbed CMZ gas. The ages of the sink particle clusters forming in the Short models are  $\sim 2.5\text{--}3.5$  Myr (Figure 9), consistent with observations of the Arches and Quintuplet clusters in the Galactic Centre. The precise ages of star clusters are impossible to determine from the simulations, both due to insufficient resolution to resolve star formation, and due to the stochastic evolution of the gas ring, which leads to a variation in sink particle cluster ages among the simulations with identical parameters.

Recent observations reveal several massive stars in the CMZ which do not belong to either of the young massive clusters (Dong et al. 2014). These stars have velocities relative to their surrounding gas ranging from  $\sim 10$  to  $\sim 80$  km/s; some of them might have formed in-situ, while others might have been ejected from parent clusters. In my models, both processes occur - some sink particles form in the dense gas filaments, representing clusters or associations too small to be resolved in the simulations; other sink particles form in clusters and then quickly leave them due to three-body interactions and tidal stripping. In order to better understand the relative importance of these processes, I plot, in Figure 17, the histogram of relative velocity between sink particles and surrounding gas (defined as the 40 nearest SPH particles, with contributions weighted by the SPH kernel) for the model Base1 at  $t = t_n = 6$  Myr. A clear peak at  $v_{\text{rel}} = 50$  km/s is visible, with  $\sim 26\%$  of the relative velocities in the range  $\{13; 78\}$  km/s (vertical dashed lines in the plot), corresponding to the minimum and maximum relative velocities observed by Dong et al. (2014). There is a large tail of high-relative-velocity sink particles, indicat-

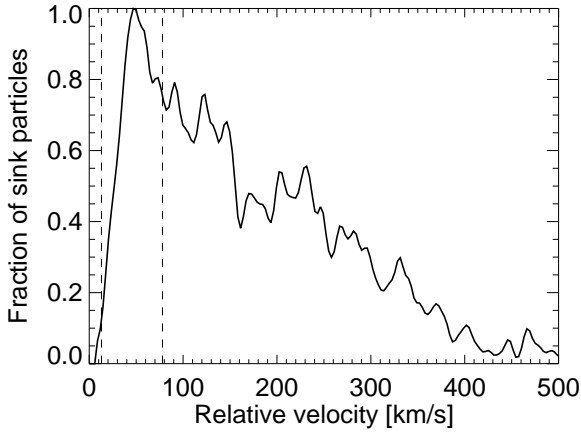


**Figure 17.** Histogram of relative velocity between sink particles and surrounding gas in model Base1. A strong peak around  $v_{\text{rel}} = 45$  km/s is present, with a power-law tail of particles escaping from newly-formed clusters. The vertical lines mark the range of relative velocities, 13 to 78 km/s, observed by Dong et al. (2014).

ing that a lot of sink particles are ejected from clusters, as one would not expect stars formed in-situ to have relative velocities larger than the background velocity dispersion  $\sigma = 150$  km/s. This may be partly a numerical effect due to insufficient detail in the star formation process in the model, as some sink particles might in reality be gas blobs which escape the clusters, disperse and do not form stars. Nevertheless, I predict that stars with significantly higher velocities relative to the surrounding gas should exist in the Galactic Centre than have been discovered so far.

Certain properties of the CMZ are not reproduced by this model. One such feature is the twist of the ring (Molinari et al. 2011), which is not seen in any of the models presented here. This suggests that the twist is either an imprint of different initial conditions, created by a different process than AGN-induced compression and fragmentation, or a much rarer effect of AGN activity than the effects that have been seen. A barred potential leads to vertical as well as radial oscillations of orbits and so could perhaps create the twisted shape required by the first two explanations (Binney et al. 1991; Hasan et al. 1993).

Another feature which the models presented here do not capture is the dynamical properties of the star clusters, i.e. their sizes, density distributions and mass functions. The lack of these properties is due to the crude star formation prescription, which only follows the initial collapse to a self-gravitating high-density core, and due to insufficient mass resolution in the models. We may expect a high integrated star formation efficiency in the cores due to the high external pressure preventing the parent molecular clouds from dispersing (Elmegreen & Efremov 1997; Zubovas et al. 2014) and a slightly top-heavy IMF due to the aforementioned high pressure (McKee & Tan 2002) and the gas dynamics being similar to the collect-and-collapse model of induced star formation (Whitworth et al. 1994).

## 5.2 Footprint of past Sgr A\* activity

Comparison of the results of the Base, Short and variation models allows me to put constraints on the past activity of Sgr A\*. The AGN episode 6 Myr ago cannot have been much weaker than Eddington-limited and cannot have lasted much less, or much longer, than 0.7–1 Myr. These results are consistent with the constraints provided by the existence of the *Fermi* bubbles (Zubovas et al. 2011; Zubovas & Nayakshin 2012) and the presence of a 6 Myr old nuclear star cluster (Paumard et al. 2006), which is evidence of a star formation event and a likely AGN feeding event (Hobbs & Nayakshin 2009). Together, these pieces of evidence strongly support the argument that an Eddington-limited AGN episode occurred in the Galactic centre  $\sim 6$  Myr ago and lasted for  $\sim 0.7 - 1$  Myr. The dynamical footprints of this evidence can still be seen today, providing a glimpse into the past state of the Galaxy. Similar evidence in other galaxies may help investigate their recent evolution (see Section 5.3).

Sofue (2003) suggested that star formation in the Galactic centre might proceed in recurrent episodes, with footprints of many such episodes visible throughout the Galaxy. In his model, the North Polar Spur was formed from a starburst that occurred 15 Myr ago, and the Galactic Centre Lobe is the remnant of a several-Myr old starburst. My results are consistent with this picture. A burst of AGN activity shuts off the feeding reservoir for a period of several Myr, but allows for more feeding later (see Section 5.4 below); this process may cause AGN luminosity to fluctuate in short bright bursts separated by periods of insignificant activity. Since each AGN episode may lead to compression of surrounding gas and a period of enhanced star formation, the star formation history in the Galactic centre should be composed of short bursts separated by longer periods of inactivity, exactly as suggested by Sofue (2003).

## 5.3 General properties nuclear rings affected by AGN feedback

Many galactic centres contain large amounts of dense gas arranged in rings or discs (Kormendy & Kennicutt 2004; Knapen 2005; Krips et al. 2007; Böker et al. 2008). This feature is often explained as a consequence of bar-driven inflow of material from kpc scales (Combes & Gerin 1985; Yuan & Kuo 1997; Sakamoto et al. 1999; Combes 2003; Kormendy & Kennicutt 2004; Sheth et al. 2005; Rodríguez-Fernández & Combes 2008), although there are unbarred galaxies with nuclear stellar rings (Knapen et al. 2004; Sil'chenko & Moiseev 2006). A bar-driven gas inflow process predicts several morphological features of the rings: ellipticity (since the rings follow triaxial  $x_2$  orbits; Morris & Serabyn 1996; Knapen et al. 2002; Kim et al. 2011), more massive gas clumps close to the orbit crossing (since material moves slowest there; Benedict et al. 1996) and an azimuthal gradient of star cluster ages (since star formation is triggered at the gas injection points; Falcón-Barroso et al. 2007; Böker et al. 2008). All three properties have been observed in some galaxies, but are not ubiquitous (Knapen 2005; Falcón-Barroso et al. 2007; Böker et al. 2008).

The model of AGN-induced compression of the CMZ gas presented in this paper might appear as an alternative



to the bar-driven inflow model. However, it is more appropriate to view the two models as complementary. The transport of gas into the central parts of the galaxy is mediated by bar potential or caused by minor mergers. Afterward, the nuclear gas ring is affected by both the aspherical gravitational potential and episodic AGN feedback. The latter has several important effects on such nuclear gas rings: facilitating the formation of more chaotic ring morphology, causing bursty and elevated star formation, and producing a correlation between star cluster ages and ring sizes.

### 5.3.1 Ring morphology

An AGN outflow disturbs the gas ring radially and induces instabilities. These alter the shape of the ring, making it irregular, rather than axially symmetric. This effect has been observed both directly, in NGC 613, where AGN activity is associated with disturbances in gas morphology (Falcón-Barroso et al. 2014), and can be inferred for many other galaxies, where irregular morphologies of gas rings are common (Sarzi et al. 2007; Böker et al. 2008).

The location of most massive molecular clouds is also random in the AGN-induced compression model. In our Galactic Centre, the star forming regions Sgr B and Sgr C are located close to the ends of the CMZ ellipse (Molinari et al. 2011), as predicted by a bar-driven inflow model. However, other galaxies do not show such regular structures (Knapen 2005; Sarzi et al. 2007; Falcón-Barroso et al. 2014), so a more stochastic process of generating molecular clouds is preferred there.

Finally, AGN-induced fragmentation also leads to random locations of star formation and hence to random azimuthal distribution of star cluster ages. This is called a “popcorn model”, as opposed to the “pearls on a string” model predicted by bar-driven inflows (Böker et al. 2008). In this latter model, star and cluster formation occurs predominantly at the ends of the ellipsoidal ring, where the gas from the galactic bar enters the ring; the young clusters then travel along the ring, producing an azimuthal gradient of stellar ages, with the youngest stars at the ends of the ellipse and oldest stars just upstream of those points. Many galaxies show azimuthal age gradients of star clusters in nuclear rings, but this isn’t a ubiquitous feature (Sarzi et al. 2007; Böker et al. 2008).

### 5.3.2 Star formation rates

The mass flow rate of a bar-driven gas inflow varies little over time, since the stellar bar is typically long-lived (Kim et al. 2011; Seo & Kim 2013). This results in an approximately constant star formation rate and predicts a rather uniform spread of star cluster ages. Observations, however, reveal that star formation in rings is more likely to be bursty (Allard et al. 2006; Sarzi et al. 2007), suggesting a need for episodic perturbations. AGN feedback can provide just such perturbations, increasing the SFR over the long-term average. AGN feedback also explains why the observed star formation efficiency in nuclear starbursts is much higher than in typical star-forming regions (Kennicutt 1998): AGN outflows create conditions of very high pressure around the gas ring, which prevent gas from escaping and enhance star formation (Elmegreen & Efremov 1997; Zubovas et al. 2014).

### 5.3.3 Ages of star clusters

The sequence of events at the basis of my model - AGN fuelling and outburst, mixing of gas in the nuclear ring and formation of molecular clouds and star clusters - predicts a clear difference between the age of star clusters in the nuclear ring and the time since the last significant SMBH accretion episode, which should coincide with the last star formation episode in the central few parsecs of the galaxy. Therefore, the age difference between the youngest stellar population in the nuclear star cluster (NSC) and the youngest star clusters in the nuclear gas ring can be expressed as

$$\Delta t_{\text{age}} = K t_{\text{dyn}}(R_{\text{ring}}) \propto R_{\text{ring}}/\sigma_{\text{gal}}, \quad (7)$$

where  $R_{\text{ring}}$  is the radius of the nuclear gas ring and  $\sigma_{\text{gal}}$  is the velocity dispersion in the galaxy spheroid.  $K$  is a constant, here assumed to be independent of ring properties or the larger galactic environment; this assumption is supported by the results of the Base and Short models (see Section 4.3). Using the parameters of the Milky Way, I find  $K \sim 3$ . Current observations cannot easily distinguish the youngest populations in NSCs, since those populations probably comprise only a small fraction of the total NSC mass (in our Galactic centre, the mass of stars formed in the burst 6 Myr ago is a few per cent of the total NSC mass), but in the future, it should be possible to test this correlation.

One example where this correlation can be seen is the galaxy NGC 1614, which hosts a nuclear starburst (Alonso-Herrero et al. 2001; König et al. 2013). The galaxy contains a very young NSC,  $t_{\text{age,NSC}} = (7 \pm 1) \times 10^6$  yr (de Grijs et al. 2005); its central velocity dispersion is  $\sigma_{\text{gal}} = 164 \pm 8$  km/s (Hinz & Rieke 2006). The nuclear gas ring extends radially from 100 to 350 pc (Xu et al. 2014), with most star-forming clumps found at a radius  $R_{\text{ring}} = 230$  pc. Using equation (7) above and  $K = 3$  gives  $\Delta t_{\text{age,NGC1614}} = 4.2$  Myr, i.e. the star clusters in the nuclear gas ring should be  $\sim 2.8$  Myr old. The precise ages of the star clusters in the nuclear ring are not known, but the presence of large HII regions and evidence of ongoing star formation suggests that they are younger than 5 Myr (Alonso-Herrero et al. 2002), consistent with the model prediction. In fact, there is evidence that the nuclear starburst in NGC 1614 is propagating outward (Alonso-Herrero et al. 2001), which may simply be a result of longer dynamical time, and hence slower evolution of a perturbed gas ring, at larger radii. This explanation predicts an apparent outward propagation of the starburst with velocity  $v_{\text{out}} = \sigma_{\text{gal}}/K \sim 55$  km/s, in excellent agreement with observations ( $v_{\text{out,obs}} = 60$  km/s Alonso-Herrero et al. 2001).

The fact that a burst of nuclear star formation follows the AGN activity episode with a delay gives an opportunity to put constraints on possible past AGN activity in a galaxy. This was discussed for our Galaxy in Section 5.2 above. An interesting example is M82, the prototypical starburst galaxy. It contains a large number of young star clusters in its  $\sim 250$  pc core, with ages  $\sim 10$  Myr (Satyapal et al. 1997; Melo et al. 2005). The velocity dispersion in the bulge of M82 is  $\sigma \approx 100 \pm 20$  km/s (Gaffney et al. 1993). Assuming that the core is a ring-like structure, the time since the most recent AGN burst should be 17.5 Myr or so - long enough for the AGN to have switched off and its most direct effects to have faded, but short enough for an outflow to remain

visible (King et al. 2011). A part of the outflow observed in M82 may be a fossil AGN outflow, rather than purely due to starburst activity. On the other hand, if one assumes that the star formation propagates inwards from the larger-scale older starburst (de Grijs 2001), the time delay between the young star cluster ages and AGN outburst implies a powerful AGN activity episode starting  $5 \pm 2.5$  Myr ago; one might expect obvious evidence of recent powerful AGN activity in this case, which is not detected (only a low-luminosity AGN is detected in M82; Matsumoto & Tsuru 1999). The outward propagation of the starburst is also supported by observations of young star cluster ages, giving a propagation velocity  $\sim 50$  km/s (Satyapal et al. 1997), qualitatively consistent with the model of an AGN-induced starburst.

#### 5.4 AGN fuelling

Although this is not the primary goal of the paper, the results presented herein offer several suggestions regarding fuelling of AGN in the presence of feedback.

The usual mechanism invoked for transporting gas from outer regions of galaxies toward the centre is gravitational torques from stellar bars (Combes 2003, also see Section 5.3 above). However, they tend to cause gas to accumulate in nuclear rings several hundred pc in size. Further gas infall is thwarted by the bar resonances and change of orbit types (Regan & Teuben 2003; García-Burillo et al. 2005). One possible mechanism for bringing gas closer to the AGN is by action of nested bars (Shlosman et al. 1989; Maciejewski et al. 2002), but only a few galaxies show evidence for such structures. Other explanations invoke transient effects, such as increased gas turbulence due to starburst activity in the central kiloparsec, which enhances mixing of gas of different angular momentum and allows gas to penetrate further into the galactic centre (Hobbs et al. 2011).

My results show that mixing of gas angular momentum can be achieved by the AGN itself, by means of feedback acting upon gas of spatially varying angular momentum (see Figure 10 and Section 4.2.3). In the case of the CMZ, this mixing is not very efficient, because gas is already in ordered motion around the centre, i.e. the mean angular momentum of the gas is large and the formal circularization radius of the whole CMZ is also large. This allows only a small fraction of all the gas to lose most of its angular momentum via the action of local gravitational torques produced by gravitational instabilities in the CMZ. In a more general case, where gas is falling in through the bulge, the motion is generally less ordered and the total angular momentum of the gas is small. In that case, mixing of gas, enhanced by AGN feedback, can cause gas clouds with very different angular momenta to collide and fall toward the centre. This scenario was investigated analytically by Dehnen & King (2013), who found that SMBHs can easily be fed at their Eddington limit by repeated short bursts of feedback. The results of my models, showing efficient angular momentum mixing, are consistent with the basic picture of this work. In particular, this irregular mixing might lead to massive reservoirs of gas accumulating very close to the SMBH, within the sphere of influence. This might be the case in Andromeda, where the double nucleus shows a massive reservoir of gas within a few

pc of the SMBH, but with little star formation (Tremaine 1995; Bender et al. 2005).

#### 5.5 Outstanding issues

The study presented here is a first step in understanding the effects of AGN activity upon nuclear gas rings. As a result, a number of simplifying assumptions had to be made in order to isolate the salient effects. Below, I discuss the importance of the effects neglected by making these assumptions.

##### 5.5.1 Gas equation of state

The models presented in this paper adopt a realistic gas heating-cooling prescription above  $T = 10^4$  K, but prevent gas from cooling below this value. This is done because cooling above  $10^4$  K is less dependent upon detailed effects of gas self-shielding, which my models cannot resolve. In principle, the temperature floor stabilizes the disc against gravitational instabilities and washes out possible small-scale structures in the perturbed gas rings, leading to a lower fragmentation rate than might be expected if the gas was allowed to cool to lower temperatures. Since the density threshold for fragmentation varies as  $n_J \propto T^3$  (eq. 5), a temperature floor at  $T = 100$  K would reduce this threshold by a factor  $10^6$ . However, the peaks in the gas density distribution are extremely sharp and tall, rising more than 6 orders of magnitude above the typical densities in the gas disc/ring. Therefore, even such a significant change in the temperature floor should not affect the fragmentation rate significantly.

Feedback from star formation might also affect the fragmentation rate, since stars can heat their surroundings and hamper or shut off further fragmentation in their vicinity (Bate 2009)). Proper implementation of feedback, however, requires much higher mass resolution than in the simulations presented here, sufficient to resolve massive stars and small stellar associations.

##### 5.5.2 Gravitational potential

The set up of the models presented in this paper makes an assumption of a spherically symmetric background potential. The presence of a Galactic bar (Bissantz & Gerhard 2002; Babusiaux & Gilmore 2005) makes the actual potential triaxial, which may significantly affect the results of these simulations. Qualitatively, an asymmetric potential should enhance the asymmetry in the final gas distribution, so the main findings of this paper should still be valid.

##### 5.5.3 Initial conditions

The initial gas distribution used in the simulations presented here is necessarily strongly idealised. One reason for choosing a smooth disc, rather than a realistic lumpy distribution, is that any enhancement of gas fragmentation is likely to be even stronger when more realistic gas distributions are considered. This would occur because a realistic gas distribution has pre-existing clumps and density inhomogeneities, which would be enhanced by a passing AGN outflow. On the other hand, some parts of the disc may be cleared, rather than

compressed, so the induced star formation rate would be smaller in a more realistic situation.

Given that most of the outflow impacting the CMZ is deflected perpendicularly, it might seem that the outflow has only a weak effect on the Galaxy on kpc scales. This was found in some previous simulations of high-redshift, therefore gas-rich galaxies (Gabor & Bournaud 2014). However, one has to keep in mind that even though the outflow is collimated, its opening angle is still large, of order  $\pi/2$  for each cone (Zubovas & Nayakshin 2012). This value is consistent with recent observational results (Nardini et al. 2015). Therefore, a large part of the galaxy is affected by the outflow directly (radially), and the rest of the gas may be compressed perpendicularly (Silk 2005; Gaibler et al. 2012; Zubovas et al. 2013). If the initial conditions are made more realistic, the outflow might escape in even more directions, leading to an even larger effect on the host galaxy.

#### 5.5.4 Numerical resolution

Another important aspect of the simulation is the numerical resolution. With the resolution chosen for the simulations, the smoothing length of CMZ gas particles,  $h_{\text{SPH}}$ , is between 0.1 – 2 times the scale height of the disc at the beginning of the simulation, with values  $h_{\text{SPH}} > H_{\text{CMZ}}$  reached only on the surface of the disc. This means that the vertical thickness of the CMZ disc is typically resolved with a few tens of particles, making the vertical structure marginally resolved, and hence fragmentation in the disc should not be artificially suppressed (Nelson 2006).

The masses of fragments forming in the CMZ depend only weakly on numerical resolution. While initially they form from single SPH particles, they quickly accrete and/or merge with other particles, growing in mass to several hundred times the SPH particle mass. Therefore, the masses of those fragments are generally resolved, from a purely numerical perspective. Their masses would undoubtedly be affected if additional physics (such as stellar feedback) is added to the simulation.

Numerical resolution also affects the interaction between the AGN wind and the CMZ gas. The momentum and energy carried by each virtual particle is scaled to the total SPH particle number, so this direct interaction should not be strongly affected. However, the effective boundary of the CMZ disc, where gas can absorb the wind energy and evaporate vertically, is always  $\sim h_{\text{CMZ}}$  thick, since virtual particles are typically absorbed in a region of this length scale. Therefore, with higher resolution, this boundary becomes physically thinner and less dense. This leads to less evaporation from the disc, but more importantly, the gas is heated to higher temperatures by the interaction with the AGN wind. Therefore, it cools more slowly (since  $t_{\text{cool}} \propto T^{1/2}$  for Bremsstrahlung cooling, dominant at the large temperatures relevant in this case) and both evaporates and passes energy to the surrounding matter more rapidly. As a result, the disc might expand more both in the radial and vertical directions. Given that this effect depends not just on resolution, but also on the gas heating-cooling prescription, a thorough analysis is beyond the scope of this paper.

## 6 CONCLUSION

I presented the results of hydrodynamical simulations of a brief AGN activity episode and the associated outflow affecting the gas disc around the Galactic centre. The simulation set up is designed to mimic the properties of our Galaxy, and the time since the AGN outburst, 6 Myr, is fixed by the age of the young stars in the central parsec. The initial distribution of the gas has the size and mass of the Central Molecular Zone, but is distributed in a smooth disc.

With this setup, I show that an Eddington-limited AGN outburst lasting for 0.7 – 1 Myr can by itself transform the smooth gas disc into a narrow, elliptical and off-centre ring of dense gas clumps and young star clusters. The masses of star-forming regions and star clusters agree rather well with the observed features in the CMZ - the Sgr B2 molecular cloud and the Arches and Quintuplet star clusters - and the shape of the ring is also similar to observations. However, the stochastic nature of gravitational instabilities, which cause the formation of structures, means that there is a lot of variation among the models and more concrete predictions are difficult to make.

Several properties of the CMZ cannot be explained with this model. Most importantly, the CMZ is known to be twisted perpendicularly to its plane, a feature not reproduced in any of my simulations. This twist may potentially be explained by the action of an asymmetric background potential, i.e. the Milky Way bar, but further work is required to test this hypothesis. Certain other observed features of the CMZ are consistent with a purely bar-driven gas inflow model. A recent AGN outburst and associated outflow should be considered as an addition to this model, not a replacement. In the future, I plan to model the response of a more realistic barred galactic environment to an AGN outflow.

Given that past AGN activity can explain many features of the CMZ, these features can be used to constrain the duration and luminosity of the AGN episode. These constraints agree with previous constraints based on the *Fermi* bubbles (Zubovas et al. 2011; Zubovas & Nayakshin 2012). Together, these aspects are dynamical footprints of past AGN activity, and point to the possibility of investigating activity history in other galaxies as well, by finding appropriate dynamical structure that might have been affected by past AGN outflows.

Nuclear gas rings and star formation within them is a common feature in many galaxies. While bar-driven gas inflows can explain many features of these rings, some aspects, such as high star formation efficiencies during repeated starbursts, disturbed morphologies and radial gradients of star cluster ages, can be more easily explained by the action of AGN outbursts. Overall, AGN outbursts have a significant influence upon the properties of host galaxy centres, and future observations will help quantify this influence.

## ACKNOWLEDGMENTS

I thank Vladas Vansevicius, Donatas Narbutis and Sergei Nayakshin for useful discussions during the preparation of this manuscript, and the anonymous referee for a thorough and helpful report. This research is funded by the Research

Council of Lithuania grant no. MIP-062/2013. Some numerical simulations presented in this work were performed on resources at the High Performance Computing Center HPC Sauletekis in Vilnius University Faculty of Physics.

## REFERENCES

- Allard E. L., Knapen J. H., Peletier R. F., Sarzi M., 2006, *MNRAS*, 371, 1087
- Alonso-Herrero A., Engelbracht C. W., Rieke M. J., Rieke G. H., Quillen A. C., 2001, *ApJ*, 546, 952
- Alonso-Herrero A., Rieke G. H., Rieke M. J., Scoville N. Z., 2002, *AJ*, 124, 166
- Babusiaux C., Gilmore G., 2005, *MNRAS*, 358, 1309
- Bate M. R., 2009, *MNRAS*, 392, 1363
- Bender R., Kormendy J., Bower G., Green R., Thomas J., Danks A. C., Gull T., Hutchings J. B., Joseph C. L., Kaiser M. E., Lauer T. R., Nelson C. H., Richstone D., Weistrop D., Woodgate B., 2005, *ApJ*, 631, 280
- Benedict G. F., Smith B. J., Kenney J. D. P., 1996, *AJ*, 112, 1318
- Binney J., Gerhard O. E., Stark A. A., Bally J., Uchida K. I., 1991, *MNRAS*, 252, 210
- Bissantz N., Gerhard O., 2002, *MNRAS*, 330, 591
- Böker T., Falcón-Barroso J., Schinnerer E., Knapen J. H., Ryder S., 2008, *AJ*, 135, 479
- Bower G. C., Wright M. C. H., Falcke H., Backer D. C., 2003, *ApJ*, 588, 331
- Cicone C., Maiolino R., Gallerani S., Neri R., Ferrara A., Sturm E., Fiore F., Piconcelli E., Feruglio C., 2015, *A&A*, 574, A14
- Cicone C., Maiolino R., Sturm E., Graciá-Carpio J., Feruglio C., Neri R., Aalto S., Davies R., Fiore F., Fischer J., et al. 2014, *A&A*, 562, A21
- Combes F., 2003, in Collin S., Combes F., Shlosman I., eds, *Active Galactic Nuclei: From Central Engine to Host Galaxy Vol. 290 of Astronomical Society of the Pacific Conference Series*, AGN Fueling: The observational point of view. p. 411
- Combes F., Gerin M., 1985, *A&A*, 150, 327
- Costa T., Sijacki D., Haehnelt M. G., 2014, *MNRAS*, 444, 2355
- Costa T., Sijacki D., Haehnelt M. G., 2015, *MNRAS*, 448, L30
- de Grijs R., 2001, *Astronomy and Geophysics*, 42, 12
- de Grijs R., Wilkinson M. I., Tadhunter C. N., 2005, *MNRAS*, 361, 311
- Dehnen W., King A., 2013, *ApJL*, 777, L28
- Dong H., Mauerhan J., Morris M. R., Wang Q. D., Cotera A., 2014, *ArXiv e-prints*
- Elmegreen B. G., Efremov Y. N., 1997, *ApJ*, 480, 235
- Falcón-Barroso J., Böker T., Schinnerer E., Knapen J. H., Ryder S., 2007, *The Messenger*, 130, 40
- Falcón-Barroso J., Ramos Almeida C., Böker T., Schinnerer E., Knapen J. H., Lançon A., Ryder S., 2014, *MNRAS*, 438, 329
- Faucher-Giguère C.-A., Quataert E., 2012, *MNRAS*, 425, 605
- Figier D. F., McLean I. S., Morris M., 1999, *ApJ*, 514, 202
- Figier D. F., Najarro F., Gilmore D., Morris M., Kim S. S., Serabyn E., McLean I. S., Gilbert A. M., Graham J. R., Larkin J. E., Levenson N. A., Teplitz H. I., 2002, *ApJ*, 581, 258
- Gabor J. M., Bournaud F., 2014, *MNRAS*, 441, 1615
- Gaffney N. I., Lester D. F., Telesco C. M., 1993, *ApJL*, 407, L57
- Gaibler V., Khochfar S., Krause M., Silk J., 2012, *MNRAS*, 425, 438
- Gando Ryu S., Nobukawa M., Nakashima S., Tsuru T. G., Koyama K., Uchiyama H., 2012, *ArXiv e-prints*
- García-Burillo S., Combes F., Schinnerer E., Boone F., Hunt L. K., 2005, *A&A*, 441, 1011
- Ghez A. M., Salim S., Weinberg N. N., Lu J. R., Do T., Dunn J. K., Matthews K., Morris M. R., Yelda S., Becklin E. E., Kremenek T., Milosavljevic M., Naiman J., 2008, *ApJ*, 689, 1044
- Gillessen S., Eisenhauer F., Trippe S., Alexander T., Genzel R., Martins F., Ott T., 2009, *ApJ*, 692, 1075
- Guo F., Mathews W. G., 2012, *ApJ*, 756, 181
- Hasan H., Pfenniger D., Norman C., 1993, *ApJ*, 409, 91
- Hinz J. L., Rieke G. H., 2006, *ApJ*, 646, 872
- Hobbs A., Nayakshin S., 2009, *MNRAS*, 394, 191
- Hobbs A., Nayakshin S., Power C., King A., 2011, *MNRAS*, 413, 2633
- Immer K., Schuller F., Omont A., Menten K. M., 2012, *A&A*, 537, A121
- Jones P. A., Burton M. G., Cunningham M. R., Requena-Torres M. A., Menten K. M., Schilke P., Belloche A., Leurini S., Martín-Pintado J., Ott J., Walsh A. J., 2011, *MNRAS*, p. 1895
- Kalberla P. M. W., Dedes L., 2008, *A&A*, 487, 951
- Kennicutt Jr. R. C., 1998, *ApJ*, 498, 541
- Kim S. S., Saitoh T. R., Jeon M., Figer D. F., Merritt D., Wada K., 2011, *ApJL*, 735, L11
- King A., 2003, *ApJL*, 596, L27
- King A. R., 2010, *MNRAS*, 402, 1516
- King A. R., Zubovas K., Power C., 2011, *MNRAS*, 415, L6
- Knapen J. H., 2005, *A&A*, 429, 141
- Knapen J. H., Pérez-Ramírez D., Laine S., 2002, *MNRAS*, 337, 808
- Knapen J. H., Whyte L. F., de Blok W. J. G., van der Hulst J. M., 2004, *A&A*, 423, 481
- König S., Aalto S., Müller S., Beswick R. J., Gallagher J. S., 2013, *A&A*, 553, A72
- Kormendy J., Kennicutt Jr. R. C., 2004, *ARA&A*, 42, 603
- Kormendy J., Richstone D., 1995, *ARA&A*, 33, 581
- Krips M., Neri R., García-Burillo S., Combes F., Schinnerer E., Baker A. J., Eckart A., Boone F., Hunt L., Leon S., Tacconi L. J., 2007, *A&A*, 468, L63
- Longmore S. N., Bally J., Testi L., Purcell C. R., Walsh A. J., Bressert E., Pestalozzi M., Molinari S., Ott J., Cortese L., Battersby C., Murray N., Lee E., Kruijssen J. M. D., Schisano E., Elia D., 2013, *MNRAS*, 429, 987
- Maciejewski W., Teuben P. J., Sparke L. S., Stone J. M., 2002, *MNRAS*, 329, 502
- Magorrian J., Tremaine S., Richstone D., Bender R., Bower G., Dressler A., Faber S. M., Gebhardt K., Green R., Grillmair C., Kormendy J., Lauer T., 1998, *AJ*, 115, 2285
- Marrone D. P., Moran J. M., Zhao J.-H., Rao R., 2006, *ApJ*, 640, 308
- Martins F., Hillier D. J., Paumard T., Eisenhauer F., Ott T., Genzel R., 2008, *A&A*, 478, 219
- Matsumoto H., Tsuru T. G., 1999, *PASJ*, 51, 321

- McKee C. F., Tan J. C., 2002, *Nature*, 416, 59
- Melia F., Falcke H., 2001, *ARA&A*, 39, 309
- Melo V. P., Muñoz-Tuñón C., Maíz-Apellániz J., Tenorio-Tagle G., 2005, *ApJ*, 619, 270
- Molinari S., Bally J., Noriega-Crespo A., Compiègne M., Bernard J. P., Paradis D., Martin P., Testi L., Barlow M., Moore T., et al. 2011, *ApJL*, 735, L33
- Morris M., Serabyn E., 1996, *ARA&A*, 34, 645
- Nardini E., Reeves J. N., Gofford J., Harrison F. A., Risaliti G., Braitto V., Costa M. T., Matzeu G. A., Walton D. J., Behar E., et al. 2015, *Science*, 347, 860
- Nayakshin S., 2014, *MNRAS*, 437, 2404
- Nayakshin S., Wilkinson M. I., King A., 2009, *MNRAS*, 398, L54
- Nelson A. F., 2006, *MNRAS*, 373, 1039
- Paumard T., Genzel R., Martins F., Nayakshin S., Beloborodov A. M., Levin Y., Trippe S., Eisenhauer F., Ott T., Gillessen S., Abuter R., Cuadra J., Alexander T., Sternberg A., 2006, *ApJ*, 643, 1011
- Pierce-Price D., Richer J. S., Greaves J. S., Holland W. S., Jenness T., Lasenby A. N., White G. J., Matthews H. E., Ward-Thompson D., Dent W. R. F., Zylka R., Mezger P., Hasegawa T., Oka T., Omont A., Gilmore G., 2000, *ApJL*, 545, L121
- Portegies Zwart S. F., Makino J., McMillan S. L. W., Hut P., 2002, *ApJ*, 565, 265
- Rathborne J. M., Longmore S. N., Jackson J. M., Kruijssen J. M. D., Alves J. F., Bally J., Bastian N., Contreras Y., Foster J. B., Garay G., Testi L., Walsh A. J., 2014, *ArXiv e-prints*
- Regan M. W., Teuben P., 2003, *ApJ*, 582, 723
- Revnivtsev M. G., Churazov E. M., Sazonov S. Y., Sunyaev R. A., Lutovinov A. A., Gilfanov M. R., Vikhlinin A. A., Shtykovsky P. E., Pavlinsky M. N., 2004, *A&A*, 425, L49
- Rodriguez-Fernandez N. J., Combes F., 2008, *A&A*, 489, 115
- Sakamoto K., Okumura S. K., Ishizuki S., Scoville N. Z., 1999, *ApJ*, 525, 691
- Sarzi M., Allard E. L., Knapen J. H., Mazzuca L. M., 2007, *MNRAS*, 380, 949
- Satyapal S., Watson D. M., Pipher J. L., Forrest W. J., Greenhouse M. A., Smith H. A., Fischer J., Woodward C. E., 1997, *ApJ*, 483, 148
- Sazonov S. Y., Ostriker J. P., Ciotti L., Sunyaev R. A., 2005, *MNRAS*, 358, 168
- Seo W.-Y., Kim W.-T., 2013, *ApJ*, 769, 100
- Sheth K., Vogel S. N., Regan M. W., Thornley M. D., Teuben P. J., 2005, *ApJ*, 632, 217
- Shlosman I., Frank J., Begelman M. C., 1989, *Nature*, 338, 45
- Sil'chenko O. K., Moiseev A. V., 2006, *AJ*, 131, 1336
- Silk J., 2005, *MNRAS*, 364, 1337
- Sofue Y., 2003, *PASJ*, 55, 445
- Springel V., 2005, *MNRAS*, 364, 1105
- Stolte A., Ghez A. M., Morris M., Lu J. R., Brandner W., Matthews K., 2008, *ApJ*, 675, 1278
- Stolte A., Hußmann B., Morris M. R., Ghez A. M., Brandner W., Lu J. R., Clarkson W. I., Habibi M., Matthews K., 2014, *ApJ*, 789, 115
- Sturm E., González-Alfonso E., Veilleux S., Fischer J., Graciá-Carpio J., Hailey-Dunsheath S., Contursi A., Poglitsch A., et al. 2011, *ApJL*, 733, L16+
- Su M., Slatyer T. R., Finkbeiner D. P., 2010, *ApJ*, 724, 1044
- Terrier R., Ponti G., Bélanger G., Decourchelle A., Tatischeff V., Goldwurm A., Trap G., Morris M. R., Warwick R., 2010, *ApJ*, 719, 143
- Tombesi F., Cappi M., Reeves J. N., Palumbo G. G. C., Yaqoob T., Braitto V., Dadina M., 2010a, *A&A*, 521, A57+
- Tombesi F., Melendez M., Veilleux S., Reeves J. N., Gonzalez-Alfonso E., Reynolds C. S., 2015, *ArXiv e-prints*
- Tombesi F., Sambruna R. M., Reeves J. N., Braitto V., Ballo L., Gofford J., Cappi M., Mushotzky R. F., 2010b, *ApJ*, 719, 700
- Tombesi F., Tazaki F., Mushotzky R. F., Ueda Y., Cappi M., Gofford J., Reeves J. N., Guainazzi M., 2014, *MNRAS*, 443, 2154
- Tremaine S., 1995, *AJ*, 110, 628
- Wang Q. D., Nowak M. A., Markoff S. B., Baganoff F. K., Nayakshin S., Yuan F., Cuadra J., Davis J., Dexter J., Fabian A. C., Grosso N., Haggard D., Houck J., Ji L., Li Z., Neilsen J., Porquet D., Ripple F., Shcherbakov R. V., 2013, *Science*, 341, 981
- Whitworth A. P., Bhattal A. S., Chapman S. J., Disney M. J., Turner J. A., 1994, *A&A*, 290, 421
- Xu C. K., Cao C., Lu N., Gao Y., Diaz-Santos T., Herrero-Illana R., Meijerink R., Privon G., et al. 2014, *ArXiv e-prints*
- Yuan C., Kuo C.-L., 1997, *ApJ*, 486, 750
- Yusef-Zadeh F., Hewitt J. W., Arendt R. G., Whitney B., Rieke G., Wardle M., Hinz J. L., Stolovy S., Lang C. C., Burton M. G., Ramirez S., 2009, *ApJ*, 702, 178
- Zubovas K., King A., 2012, *ApJL*, 745, L34
- Zubovas K., King A. R., Nayakshin S., 2011, *MNRAS*, 415, L21
- Zubovas K., Nayakshin S., 2012, *MNRAS*, 424, 666
- Zubovas K., Nayakshin S., 2014, *MNRAS*, 440, 2625
- Zubovas K., Nayakshin S., King A., Wilkinson M., 2013, *MNRAS*, 433, 3079
- Zubovas K., Sabulis K., Naujalis R., 2014, *MNRAS*, 442, 2837